Characterization of ITS3 sensor prototypes using particle telescopes with beam and cosmics

Julija Zaksaitė

Project duration: 9 months

Supervised by David Silvermyr and Iaroslav Panasenko

May 2026

LUND UNIVERSITY

Department of Physics
Division of Particle & Nuclear Physics

Abstract

During the third long LHC shutdown (2026-2030), one of the four main experiments at CERN, ALICE, will undergo an extensive upgrade of the Inner Tracking System (ITS3). During this, the three innermost layers of the detector will be replaced by a novel technology, where wafer-scale stitched sensors will be bent into half-cylinder shape and placed one on top of the other, wrapping around the beam pipe.

This thesis presents the characterization of the sensor prototypes, called babyMOSS, in two different scenarios: using high-energy particles produced in a beam and cosmic muons. Firstly, the particle telescope set-up used in a test beam is discussed, where detection efficiency and spatial resolution were measured for different pixel sensor geometries. Secondly, the design of the babyMOSS telescope, built in Lund University is presented, with the main focus on the triggering scheme optimization and software implementations. Some of the first results of observed rate distribution, cluster size, residuals and angular distribution are also discussed.

Acknowledgments

Firstly, I would like to thank my supervisors David Silvermyr and Iaroslav Panasenko for the opportunity to work on this project and the possibility to participate at test beams at CERN, for their feedback on my thesis and overall guidance throughout the year. I have learned a lot from them and I thoroughly enjoyed the work we have done.

I would also like to thank my friends in Lund, they made the past two years so more enjoyable. I will greatly miss our lunch conversations and Wednesday pubs. A special thank you goes to Macaila for making our office such a safe and lively space.

Lastly, I am thankful for my Mom, my cousins Gabija and Monika, and my friends back in Lithuania - their constant support and care made these past two years seem easy.

ALICE A Large Ion Collider Experiment

ALPIDE ALice PIxel DEtector

BSY Busy

CC Clock Cycle

CERN The European Organisation for Nuclear Research

CH Channel

CMOS Complimentary Metal-Oxide Semiconductor

CPV Charged-Particle Veto

DAQ Data Acquisition

DUT Device Under Test

EAS Extensive Air Shower

EMCal ElectroMagnetic CALorimeter

ER Engineering Run

FHR Fake Hit Rate

FPGA Field Programmable Gate Array

HMPID High-Momentum Particle Identification Detector

HU Half-Unit

IB Inner Barrel

IP Interaction Point

ITS Inner Tracking System

LHC Large Hadron Collider

LS Long Shutdown

MAPS Monolithic Active Pixel Sensor

MIP Minimum Ionising Particle

MOSAIX MOnolithic StItched Active pIXel

MOSFET Metal-Oxide Semiconductor Field-Effect Transistor

MOSS MOnolithic Stitched Sensor

NA North Area

NA61/SHINE SPS Heavy Ion and Neutrino Experiment

OB Outer Barrel

PHOS PHOton Spectrometer

PS Proton Synchrotron

QCD Quantum Chromodynamics

QGP Quark-Gluon Plasma

RHIC Relativistic Heavy-Ion Collider

RSU Repeated Sensor Unit

STAR Solenoidal Tracker at RHIC

SPS Super Proton Synchrotron

TCP/IP Transmission Control Protocol/Internet Protocol
THR Threshold
TOF Time-Of-Flight
TPC Time-Projection Chamber
TRD Transition Radiation Detector
TRG Trigger
ZDC Zero Degree Calorimeter

Contents

1 Introduction

The Standard Model, developed in the 1970s, is a theory describing fundamental particles and their interactions. It focuses on the properties of elementary particles of four distinct types: two families of fermions of spin-$\frac{1}{2}$, known as leptons and quarks, a family of spin-1 bosons, also known as gauge bosons, who are treated as force carriers in the Standard Model, and a spin-0 particle, called the Higgs boson, which gives mass to elementary particles. These are the smallest known constituents of matter, treated as point-like, without internal structure or excited states [1]. In order to detect and study them, particle physicists have developed the most advanced and precise tools, that make use of how particles interact with matter.

Up until the early 1950s, main sources of energetic particles were cosmic rays. One of the oldest detectors used for particle track and ionisation measurements was the cloud chamber. The detector is filled with a gas-vapour mixture, in which a particle passing through ionises and leaves a trajectory, that can be photographed. By operating a cloud chamber in a strong magnetic field, Carl Anderson in 1932 discovered the positron in cosmic rays, and, in 1937, together with Neddermeyer, discovered the muon [2]. Another detection technique involved combining scintillators, that emit light when a charged particle passes, with photodetectors, such as a photomultiplier tube. This allowed for the conversion of a weak photon signal into a detectable electric impulse [1].

With the advancements in technology, accelerators became available to produce high-energy particles at high frequencies. With this, more sophisticated particle detection methods were developed. In particular, semiconductor technologies have been adapted for particle detection and measurement purposes, with silicon being the preferred material for detector fabrication. In the 1980s, first silicon strip detectors were installed and successfully used in NA11 (North Area 11) fixed target experiment at CERN. The experiment provided, for the first time, the measurement of the decay time of the D meson [3]. Since then, significant progress has been made in silicon sensor technologies. Different sensor geometries have been implemented, such as strip and pixel, to deal with the extremely high rates of the particles produced. Introduction of Monolithic Active Pixel Sensors (MAPS) marked an important milestone in precision measurements, since now the sensors could be thinned down to a few tens of micrometers, allowing for even more precise track reconstruction.

All modern high-energy particle physics experiments nowadays employ silicon detectors at some capacity. At the Large Hadron Collider (LHC) at CERN, silicon detectors are used closest to the interaction point as vertex detectors. LHC is capable of producing collisions at the highest energies ever achieved in a laboratory, up to 13.6 TeV for proton-proton collisions and up to 5.36 TeV for lead-ion collisions [4]. A Large Ion Collider Experiment (ALICE) at CERN is one of the 4 main experiments at the LHC, dedicated to studying quark-gluon plasma - a form of matter believed to have existed shortly after the Big Bang. ALICE is equipped with state of the art detection technologies, that allow to reconstruct particle collisions and their tracks, to identify particles and measure their momentum. The precision of these measurements is crucial for expanding our knowledge about the origins of the Universe.

The LHC is preparing for the Long Shutdown 3 (LS3) (2026-2030), during which a number of detector systems will undergo an upgrade. For ALICE, the most important upgrade is of the Inner Tracking System (ITS), which is the vertex detector located in the Central Barrel, closest to the interaction point. The current Inner Tracking System, known as ITS2, represents the largest use of MAPS technology, however, during the LS3, the three innermost layers of the ITS2 will be replaced by a completely novel detector system, where wafer-scale stitched silicon sensors, thinned to 50 µm will be bent into a half-cylinder shape and placed on top of each other, forming a cylinder around the beam pipe. The main improvements of the ITS3 include the reduction of the material budget by a factor of 4, as well as bringing the detector 5 mm closer to the interaction point [5].

During the first engineering run (ER1), the first stitched prototype sensors, called the MOnolithic Stitched Sensors (MOSS), were developed. The pixel detector consists of 10 repeated sensor units (RSU), which are divided into two half-units of differing geometries, allowing to study the performance of the sensors under the expected ITS3 conditions. Furthermore, a single-RSU sensor, called babyMOSS, was produced, in order to facilitate characterization studies. Currently, the second engineering run (ER2) is in progress, where the full feature prototype for the ITS3 sensor, called the MOnolithic StItched Active pIXel (MOSAIX), is studied. The goal is to fully understand and validate the sensor for the final engineering run (ER3).

This project is split into two parts. In the first one, the final ER1 test beam and its results are discussed, where a telescope, consisting of babyMOSS detectors, was used in a particle beam. The results of the test beam on detection efficiency and spatial resolution are reported. While test beams remain the most common way to characterize sensors, in the second part of this project, an alternative is proposed, using cosmic muons as a source of high-energy particles. For this purpose, a dedicated telescope was built in Lund University. Developments for the data acquisition process as well as some first results are presented.

2 Silicon Detectors

Semiconductor devices make up the basis of the modern electronics industry. Various diodes and transistors are used in mobile phones, computers, cars, etc. - most everyday electronic appliances. For high-energy physics experiments, detectors made of semiconductor materials are widely used, as they offer measurements of position, energy and time resolution at an extremely high precision. This is particularly useful at accelerator experiments, where particles of a very short lifetime interact at high rates and energies. Semiconductor detectors are mainly used as tracking detectors, in calorimeters, or in imaging Cherenkov detectors [6].

Silicon is the most widely used and researched semiconductor material for particle physics experiments, due to its low price, availability, electrical properties and radiation hardness. Silicon crystals have a band gap of $E_g = 1.12$ eV at room temperature, they have a high carrier mobility, meaning that charge collection is fast, and the crystals can be grown very pure. Furthermore, silicon has relatively low density and radiation length X_0 and it can be doped with specific materials in order to shape the potential inside the detector, making it a suitable candidate for particle and radiation detection [7].

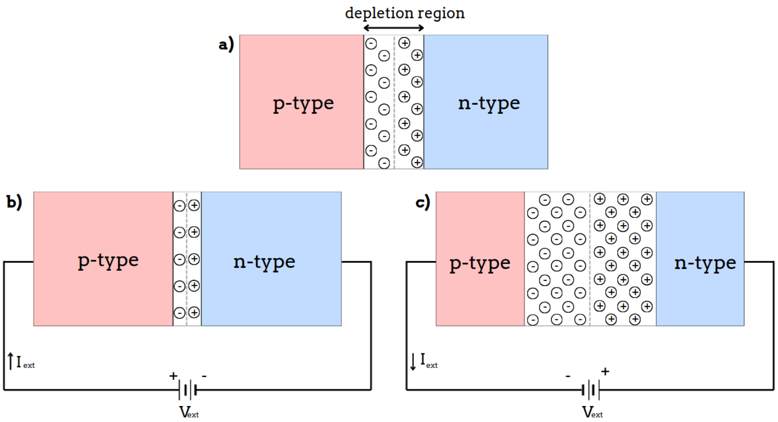

Figure 1: p-n junction a) without external voltage, b) forward biased and c) reverse biased.

To understand the functioning of semiconductor detectors, it is important to understand the basics of a p-n junction. During manufacturing, a semiconductor can be doped with different types of materials, in order to change their electrical properties: introducing a material that has a surplus of electrons creates an n-type semiconductor, whose main charge carriers are electrons, and introducing a material that has fewer valence electrons, creates a p-type semiconductor, whose main charge carriers are holes. Combining these two types of semiconductor materials produces a p-n junction. At the boundary of the junction, recombination between the different charge carriers occurs, which creates a region, known as the depletion zone. The size of the depletion region can be modified by applying a voltage to the p-n junction. Applying a forward bias (meaning that the positive voltage is applied to the p-doped side and the negative - to the n-doped side) will decrease the width of the depletion zone and applying a reverse bias will increase it, as is shown in Figure 1. In the case of semiconductor detectors, a reverse bias is usually applied in order to have the depletion zone as wide as possible. This is useful for particle detection, since a particle, passing through the depletion region, will generate electron-hole pairs that then will create a detectable signal. In an undepleted zone, the created electron-hole pairs would recombine with the charge carriers of the semiconductor and a signal would not be generated in a detector [8].

While a simple p-n junction, coupled with a read-out scheme, can be used for particle detection, more sophisticated detector geometries are employed at current high-energy experiments. The two most common structures are strip detectors and pixel detectors, shown in Figure 2. The strip sensor surface is divided into strips that have a pitch of 50-100 µm and the pixel detectors have smaller implant areas, typically having a pitch less than 100 µm [8]. The guard ring, visible in the Figure 2 a) and b), is designed to minimize the leakage current and consequently to minimize noise in the detector. The pixel

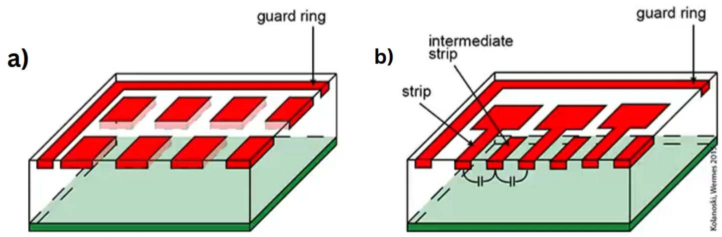

Figure 2: Possible geometries of a single sided silicon detector: a) pixel detector and b) strip detector. Sourced from [8].

detector has some advantages over the strip detector geometry, especially when it comes to incident particle track reconstruction. Pixel sensors have a better space-point resolution, being able to provide all 3 spatial coordinates of the particle track (comparing to only 1 spatial coordinate from the strip sensor). In addition, due to the small diode areas, the pixel detector has a higher signal-to-noise ratio and is able to sustain higher rates of radiation, than a strip detector [8, 9]. These properties are extremely important for experiment located at high-energy accelerator facilities, for example at the Large Hadron Collider (LHC) at CERN, where approximately 1 billion collisions occur every second [4].

2.1 Charged particle detection

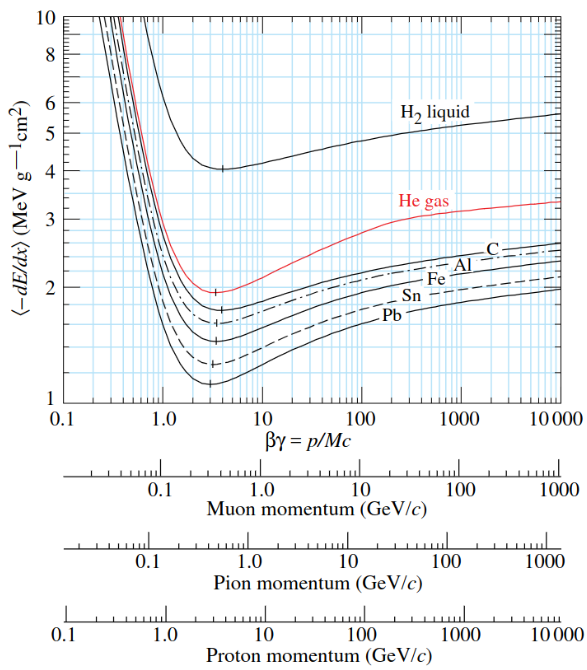

Figure 3: Mean energy loss in different matter: liquid hydrogen, gaseous helium, carbon, aluminium, iron, tin and lead. Radiation losses are not plotted. Sourced from [6].

Particle detection is based on how particle passes through matter. Here, only charged particle interactions are treated since these are the particles that can be directly detected by silicon pixel sensors. Furthermore, the discussion is focused on heavy particles, i.e. particles that are heavier than electrons, such as muons, pions, protons and others. Such particles, passing through matter interact with the nucleons and electrons of that matter. Most of these interactions are electromagnetic in nature and therefore cause energy loss of the incident particle. In general, for particles of charge z, that pass through a medium of density ρ, atomic number Z and atomic mass A, the average energy loss per unit length dx is given by the Bethe-Bloch formula [8]:

$$-\left\langle \frac{dE}{dx} \right\rangle = K\frac{\rho Z}{A}\frac{z^2}{\beta^2}\left[ln\left(\frac{2mc^2\gamma^2\beta^2}{I} - \beta^2 - \frac{\delta(\beta\gamma)}{2} - \frac{C(\beta\gamma, I)}{Z}\right)\right] \tag{1}$$

where, m is the electron mass (hit particle), I is the average ionization potential, $\beta = \frac{v}{c}$ with v being particle velocity and c speed of light, γ is the Lorentz factor and K is a constant defined as

$$K = \frac{4\pi\alpha^2(\hbar c)^2 N_A(10^3\mathrm{kg})}{mc^2} = 30.7\mathrm{keV\,m^2\,kg^{-1}}$$

The two last terms in (1) are density and shell corrections, respectively. The density correction is important at high energies, when the electric field of a particle polarizes the atoms in the matter, far from the particles path. The shell correction is important at low energies, when the velocity of the incident particle is smaller than the velocity of the bound electrons in the medium [10].

Figure 3 shows the mean energy loss, also known as the stopping power, in different matter in terms of particle momentum for muons, pions and protons. For small momentum values, the stopping power decreases rapidly with increasing energy, until it reaches a minimum. Afterwards, the mean energy loss increases slowly with the increasing momentum [7]. Particles that have mean energy loss close to the minimum are also known as minimum ionizing particles (or MIP). This is the case of most relativistic particles, such as cosmic muons.

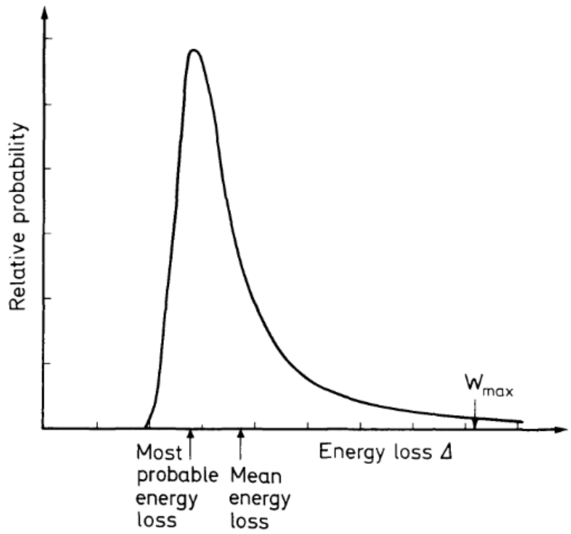

Figure 4: Energy loss distribution of a charged particle in a thin layer. Sourced from [10].

While the Bethe-Bloch formula describes the average energy loss in matter pretty well, in practice, the most probable energy loss needs to be considered. The energy loss of a heavy charged particle is affected by statistical fluctuations in the number of collisions that can occur in the medium. This is especially relevant for thin absorbers, such as silicon detectors. The energy loss distribution is best described by a Landau distribution [8], which is asymmetric and has a long tail at high energies, as is shown in Figure 4. During particle's passage through matter, different amounts of energy can be transferred to the medium, with the peak of the distribution representing the most probable value. The tail represents the possibility of an extremely large energy transfer occurring in a single collision, which is rare. Because of this, the mean energy loss does not correspond to the most probable energy loss value.

Depending on the amount of energy transferred when a particle passes through a silicon detector, a certain amount of electron-hole pairs will be created in the depleted region of the detector. For example, a minimum ionising particle, passing through a 300 µm thick silicon sensor, will create about 23000 electron-hole pairs [11]. The created electron-hole pairs in the electric field in the depletion region will move towards respective electrodes. The movement of the charges, also known as the drift current, will then induce a signal, that can be detected by the readout electronics [7, 8].

2.2 Monolithic Active Pixel Sensors

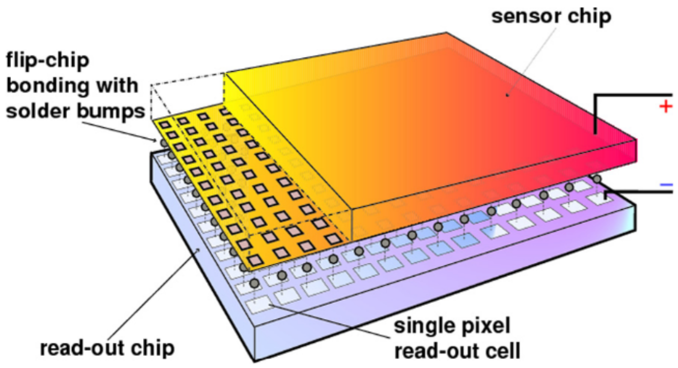

Figure 5: Hybrid pixel detector layout. Sourced from [9].

The two most common silicon pixel detector types are hybrid and monolithic. Hybrid pixel sensors are made out of two separate parts: silicon diode with a pixel cell layout and a read out chip with the same cell pattern. The two components are soldered together through a conducting micro-connection, called a bump bond, at every pixel cell, as is shown in Figure 5. Due to the dual layout of a hybrid pixel detector, it is possible to optimise the properties of the sensor and readout electronics chip separately. On the other hand, this sensor design has a quite large material thickness, which can negatively impact track reconstruction [8].

Since both the sensor and the readout chip are fabricated from silicon, with technological advancements, a new type of detector was realised in the 1990s, where both components are manufactured on one chip [8]. The detectors are now known as Monolithic Active Pixel Sensors (MAPS), built using CMOS technology[1]. The CMOS technology allows to produce light and highly granular pixel sensors with a pixel pitch in the range of 20-30 µm and a sensor thickness of 50 µm [12].

Figure 6 shows a schematic of a MAPS. A typical CMOS MAPS chip contains a highly p-doped silicon substrate, that has relatively low resistance, a moderately p-doped, highly ohmic epitaxial layer on top of it, that has different silicon structures added to it using the lithography method. These structures, also called wells or diffusions, of either p-type or n-type, contain charge collection electrodes. On top of the silicon structures, metal layers are deposited, used as electric contacts between the components [13].

The sensor has only a small depletion region created where an n-well collection diode is positioned into the epitaxial layer. However, due to the fact that the doping of the epitaxial layer is a few orders of magnitude smaller than the doping of the surrounding layers (p-wells and p-substrate), reflective potential barriers are created at the boundaries of the epitaxial layer [14]. As a consequence, when a charged particle passes through the sensor, the generated electron-hole pairs move, via diffusion, inside the epitaxial layer, towards the depletion region under the n-well. The epitaxial layer can be considered as the sensitive layer of the detector. While almost all charge carriers, released inside of the epitaxial layer, reach the collection diode before recombining, only a third of them are collected in the seed pixel, that is, the pixel which is closest to the particle impact. The others diffuse into neighboring pixels, creating a cluster [13]. The sizes of these clusters can be reduced by applying a reverse bias throughout the sensor in order to expand the depletion region.

[1]CMOS (Complementary Metal-Oxide Semiconductor) technology refers to a fabrication process of the metal-oxide semiconductor field-effect transistors (MOSFETs). The fabrication process involves combining both p-type and n-type MOSFETs in a logic circuit.

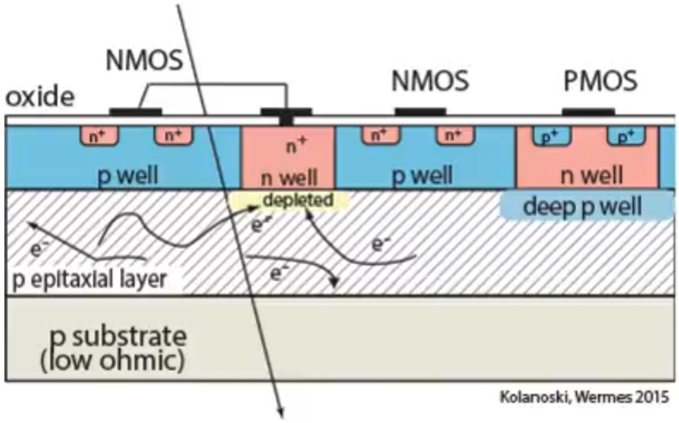

Figure 6: An example of a Monolithic Active Pixel Sensor (MAPS). Example transistors are shown in the electronics layer and the signal path is also indicated. Sourced from [8].

Overall, MAPS have an exceptional spatial resolution, low material budget, a high radiation tolerance and low power consumption, which allows the sensors to perform extremely precise track reconstruction. Therefore, they are the perfect candidates for the vertex detector and have been successfully employed in various heavy-ion collision experiments: at the RHIC at Brookhaven National Laboratory, specifically in the STAR detector (Solenoidal Tracker at RHIC) and at various experiments at CERN, such as the vertexing detector of NA61/SHINE (SPS Heavy Ion and Neutrino Experiment) and the inner tracking system of ALICE (A Large Ion Collider Experiment) [13].

3 A Large Ion Collider Experiment (ALICE)

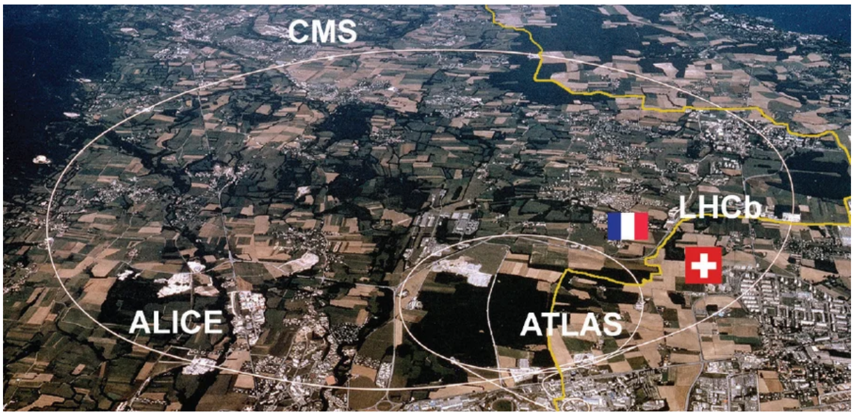

Figure 7: Map showing the location of the LHC tunnel with the 4 main experiments. Image sourced from [15].

A Large Ion Collider Experiment (ALICE) is a general-purpose, heavy-ion detector at the CERN Large Hadron Collider (LHC), taking data since 2009 [16]. It is one of the four main experiments at CERN, located on the French side of the accelerator complex, at Interaction Point 2 (IP2) (see Figure 7). The experiment is dedicated to study the physics of strongly interacting matter, specifically the nucleus-nucleus collisions, producing extremely high energy densities and temperatures, conditions at which quark-gluon plasma is formed [17]. In ALICE, the main focus is on lead-lead collisions, although collisions of lighter ions and protons are also studied.

3.1 Quark-gluon plasma

The theory that describes fundamental particles and their interaction is called the Standard Model. Specifically, interactions between quarks and gluons are described by Quantum Chromodynamics (QCD). Quarks are the fundamental particles that make up composite hadrons, such as protons and neutrons, and gluons are the strong force mediators. The theory explains that neither quarks nor gluons can be observed on their own, they can either exist as baryons (made up of 3 quarks) or as mesons (made up of a quark and an antiquark), held together by the gluons. Hadrons, such as protons and neutrons, are present in the different phases of matter: gases, liquids and solids. Quark-gluon plasma (QGP) however, is an extreme phase of matter, that filled the universe in the first ~ 10 μs after the Big Bang. The main feature of QGP, is that quarks and gluons are not bound together. They instead appear in an extremely hot and dense soup-like matter, in which the particles can move relatively freely [18]. After the Big Bang, as the QGP matter cooled down, quarks and gluons recombined, forming the particles and matter that is observed currently.

ALICE is trying to recreate the conditions of these first ~ 10 μs of the universe, in order to study QGP. This can be done by colliding heavy nuclei, for example lead, at extremely high energies, up to 5.5 TeV. Due to the fact that during these collisions, the QGP exists for an extremely short amount of time, it is impossible to observe it directly. Instead, studies of different physical observables can be done that shed light on the properties of QGP. For example, important measurements within heavy-ion collisions have been done on particle multiplicity, that provide information on the centrality of the collisions and, as a consequence, on various parameters of the system, such as energy density, or lifetime. Measurements of the mean transverse momentum of identified particles can be used to obtain the amount of radial flow

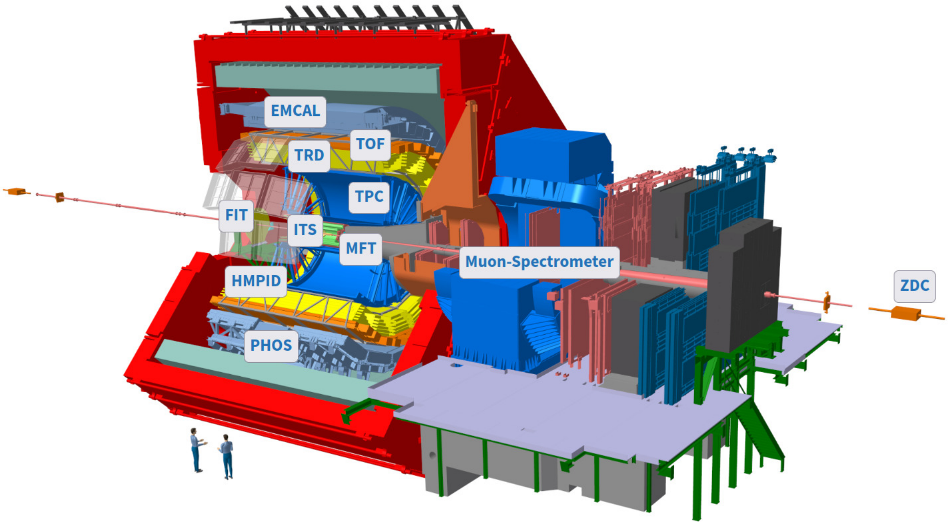

Figure 8: ALICE Detector layout. Subsystems not mentioned in text are: Zero Degree Calorimeter (ZDC), Muon Tracking Chambers, Muon Trigger Chambers, Magnets (solenoid and dipole) and absorbers. Sourced from [21].

within a system. Furthermore, measurements of strangeness (or in other words, the amount of particles with strange quarks) have been performed as the enhancement of strangeness production is one of the signatures of QGP [19].

Studying QGP will help better understand the how matter is formed and how it evolves, as well as how quarks and gluons are confined.

3.2 ALICE detectors

The ALICE detector is 26 m long, 16 m high, and 16 m wide, composed of multiple sub-detectors, that each are responsible for different physics goals. The subsystems are shown in Figure 8. The detector subsystems, located in the central barrel, are briefly outlined below [20]. The first four cover the full azimuthal angle, while the last three have a limited azimuthal acceptance.

- **Inner Tracking System (ITS)** is the tracking detector in ALICE based on pixel detectors, located between the beam pipe and the Time Projection Chamber (TPC). ITS focuses on primary vertex determination, secondary vertex reconstruction (in particularly of charm and hyperon decays), low-transverse-momentum particle tracking and identification. In addition, the detector also helps improve the momentum and angle resolution for particles that are reconstructed by the TPC. For the LHC Run 1 and Run 2, the ITS consisted of 6 cylindrical layers, based on silicon pixel detectors (2 layers), silicon drift detectors (2 layers) and silicon strip detectors (2 layers). This set-up allowed to achieve the required track impact parameter resolution.

- **Time-Projection Chamber (TPC)**, located at the central barrel, is used to reconstruct particle tracks, measure charged-particle momentum, identify particles and determine vertices. TPC subsystem has a large active gas volume and is cylindrical, having an inner radius of 0.85 m, an outer radius of 2.5 m and a length along the beam direction of 5 m [22].

- **Transition Radiation Detector (TRD)** is primarily used for electron identification in the central barrel, for momenta above 1 GeV/c. In addition, it acts as a fast trigger for charged particles with high momentum. TRD is composed of a total of 522 detectors arranged in a cylindrical shape, of 7 m diameter and 7 m length. TRD, in combination with the ITS and TPC, provides the possibility to study the production of light and heavy vector-meson resonances in heavy-ion collisions [23].

- **Time-Of-Flight (TOF) detector** is responsible for particle identification in the intermediate momentum range: below 2.5 GeV/c for pions and kaons, up to 4 GeV/c for protons. In particular, TOF is used to determine the time it takes for a particle to travel from the vertex, to the TOF detector, in order to measure the particle's speed. The detector is located about 3.7 m from the interaction point and has a cylindrical array with an active area of $\sim$ 141 m^2 [24].
- **High-Momentum Particle Identification Detector (HMPID)** is a Ring imaging Cherenkov detector, that consists of 7 modules of 1.4 $\times$ 1.3 m^2 each. HMPID can identify charged particles (pions, kaons and protons) that have large momentum, above the momentum reached through energy-loss in ITS and TPC, and time-of-flight measurements in TOF. This information is then used to better understand the nuclear matter, produced at very energetic heavy-ion collisions [25].
- **PHOton Spectrometer (PHOS)** is a high-resolution electromagnetic spectrometer, used to search for electromagnetic radiation coming from the strongly interacting matter in nucleus-nucleus collisions. In addition, it provides measurements of the hadron spectra via their radiative decays. The spectrometer consists of an electromagnetic calorimeter (PHOS) and a Charged-Particle Veto (CPV) detector, that helps with photon identification. In addition, PHOS is used as a trigger detector, to help with high-energy photon event selection [26].
- **ElectroMagnetic CALorimeter (EMCal)** is a lead-scintillator sampling calorimeter, located next to the ALICE magnet coil, $\sim$4.5 m away from the beam line. It is responsible for measuring highly energetic photons, electrons, neutral pions, and jets of particles, as well as correlations between them [27].

The following sections focus on the current inner tracking system and introduce the ITS3 upgrade.

3.3 Inner Tracking System 2

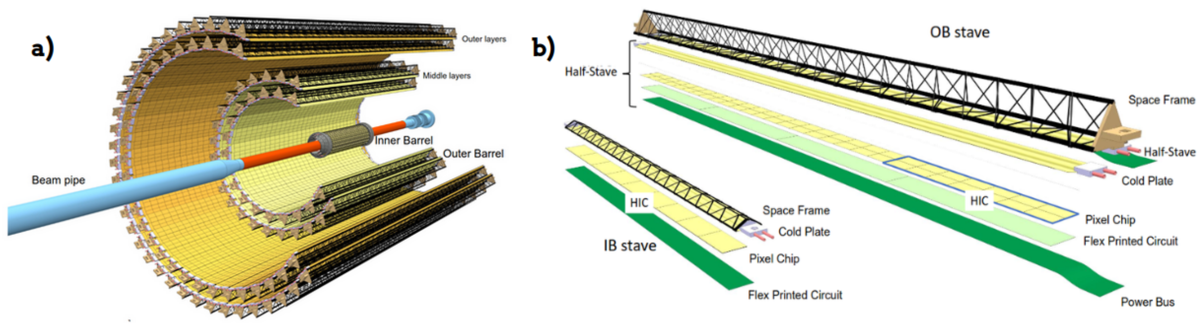

Figure 9: Inner Tracking System 2 of ALICE, a) shows the schematic layout of ITS2 and b) shows the inner and outer barrel stave layout. Source from [28].

The current inner tracking system in ALICE is called ITS2 and was installed during the LHC Long Shutdown 2 (2019-2022). The detector consists of 7 layers: 3 layers of the inner barrel (IB) and 2 double layers of the outer barrel (OB), as can be seen in Figure 9 a). The layers themselves are made out of staves - basic detector units consisting of a hybrid integrated circuit, on which pixel chips are bonded (9 chips for IB, 14 chips for OB), a coldplate and a space frame, used for mechanical support, as can be seen in Figure 9 b) [28].

ITS2 is based on the MAPS technology. It consists of 15 $\times$ 30 mm^2 chips developed by ALICE, called ALPIDE (ALice PIxel DEtector). The chips comprise a total active area of 10 m^2 and a total of 12.5 $\times$ 10^9 pixels, corresponding to the largest scale MAPS application in a high-energy physics experiment [29]. The ALPIDE sensor has high integration density, low power consumption, about 40 nW per pixel, as well as solid radiation hardness, with regards to previous generation of MAPS [30, 31]. Compared to the previous ITS detector, improvements have been made in measured position resolution and the reduction of the material budget from 1.14% X_0 per layer down to 0.36% X_0 per layer for the inner barrel and 1.1% X_0 per layer for the outer barrel. In addition, the distance to the interaction point of the innermost layer was reduced from 39 mm down to 24 mm. The read-out rates also went up to 50 kHz for Pb-Pb collisions and up to 400 kHz for proton-proton collisions [28].

The ITS2 upgrade was able to improve the precision of the primary and heavy-flavour hadron decay vertex reconstructions, as well as make it possible to reconstruct particle tracks before they undergo weak decay, solely using the Inner Tracking System. Furthermore, tracking efficiency for particles with momentum below 1 GeV/c increased 8 times [32].

3.4 Upgrade of the Inner Tracking System - ITS3

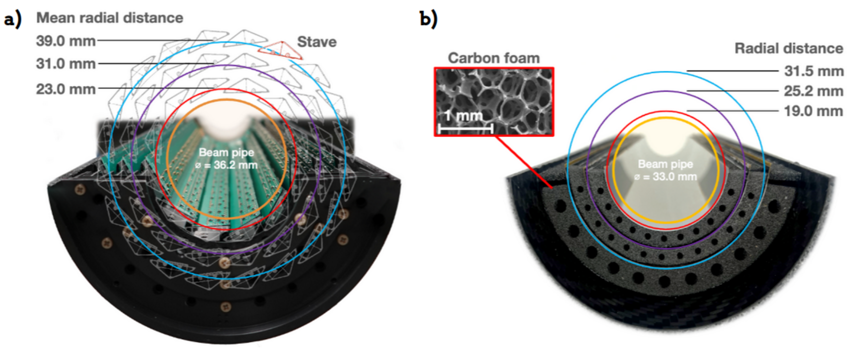

Figure 10: Comparison of radial cuts between a) the current ITS2 and b) a model of ITS3. Sourced from [33].

During the Long Shutdown 3 of the LHC, planned to take place 2026-2030, the 3 innermost layers of the Inner Tracking System will be replaced by wafer-scale silicon sensors, thinned out to ~ 50 µm and bent to a cylindrical shape. Figure 10 shows the comparison of the radial cuts of the ITS2 in 10 a), and a model for the ITS3 in 10 b). The staves, that are assembled together to create a half-cylinder shape will be replaced by a single sensor. The layers of the inner barrel will be held in place using carbon foam and cooled by a forced airflow [5].

A novel stitching technology will be applied to connect reticles on a wafer at the production stage, allowing fabricating wafer-scale sensors, of area 10×27 cm^2 [30]. The silicon sensors will be bent to a half-cylinder shape, while maintaining both their mechanical and electrical properties. A single layer of the inner barrel will consist of 2 half-cylinder sensors, placed one on top of the other, as can be seen in Figure 11.

The main improvements of the ITS3 involve minimizing the material budget and reducing the distance to the interaction point. Specifically, the material budget will go from 0.36% X_0 down to 0.09% X_0 per layer. In addition, the inner barrel will move 5 mm closer to the interaction point (for the innermost layer, this distance is reduced from 24 mm down to 19 mm) [5, 34].

The ITS3 upgrade will significantly improve the performance of the Inner Tracking System. The track impact resolution parameter is expected to improve by a factor of 2 and the track resolution efficiency is expected to improve for low-transverse momentum particles. This will significantly advance the measurements of heavy-flavour hadrons, which will in turn provide a deeper insight into the quark-gluon plasma and its formation [5].

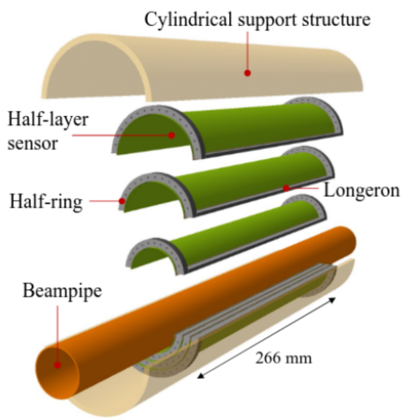

Figure 11: Simplified layout of the inner barrel of the ITS3. Sourced from [5].

3.4.1 Pixel Sensor Prototypes

The first prototype fabricated for ALICE ITS3 pixel sensor development in the Engineering Run 1 (ER1), shown in Figure 12 a), is called the MOnolithic Stitched Sensor (MOSS), designed in a 65 nm CMOS Imaging technology. It is a 1.4×25.9 cm^2 stitched silicon sensor, consisting of 10 repeated sensor units (RSU) and 2 smaller end-cap regions on both extremities, for a total of 6.72 million pixels [5]. The main goal of the prototype is to better understand the stitching process and to be able to evaluate the performance of the pixel matrix under the ITS3 operating conditions [35].

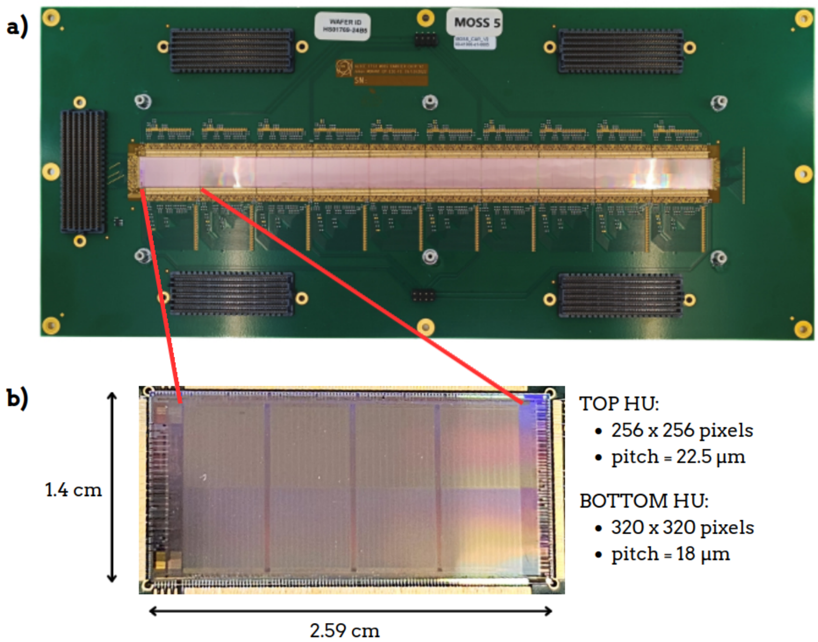

Figure 12: Sensor prototypes for ER1 where a) MOnolithic Stitched Sensor (MOSS) on a carrier board (sourced from [36]) and b) single-RSU sensor known as babyMOSS.

A single-RSU sensor is called a babyMOSS, also visible in Figure 12 b). It was fabricated to facilitate test beam studies and its characterization is the main focus of this project. A single babyMOSS sensor consists of a Right End Cap (REC), a Left-End Cap (LEC), and 2 half-units (HU) that have independent powering, readout and control. Each HU is separated into 4 matrices, also called regions, of slightly differing in-pixel analog electronics design. This allows to study each regions response, as well as potential optimization for future prototypes [34].

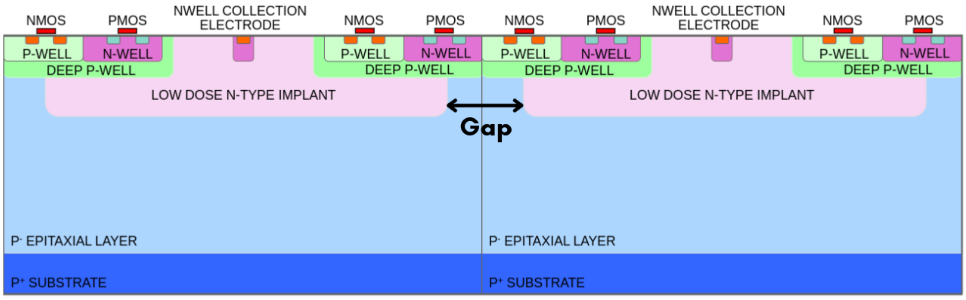

Figure 13: MOSS (BabyMOSS) sensor cross section of two pixels with a gap in between them. Sourced from [5]

.

The 2 HUs differ in their geometry: the top HU is made up of 4 regions of 256×256 pixels of 22.5 µm pitch and the bottom HU consists of 4 regions of 320×320 pixels of 18 µm pitch. Studying different integration densities allows for an in-depth characterization of the prototypes [34].

A cross section of the pixel sensor is shown in Figure 13. The pixel contains a low-doped, deep n-type implant in the pixel region, containing a gap at the pixel boundaries. Introducing the gap reduces charge sharing in-between two neighbouring pixels. In fact, due to the electrical field created in the pixel, the charge carriers near the pixel borders drift towards the collection diodes, thereby increasing the charge collected by a single pixel [37, 38]. Therefore, two different splits of the babyMOSS sensor have been manufactured, with the main difference being the gap size for the larger pixel pitch regions (top HUs): split 1 has a gap size between n-type implants of 2.5 µm and split 2 has a gap size of 5 µm. For the bottom HU, the gap size is 2.5 µm for chips of both splits.

The babyMOSS sensor has been thoroughly characterized in various test beam campaigns, from 2023 up to 2025. Set-up and results of the latest test beam, showing detection efficiency and spatial resolution studies for babyMOSS sensors of different splits is presented in chapters 4 and 5. Furthermore, an additional possibility for sensor characterization can be implemented, utilizing cosmic muons, which allows for a year-round data acquisition outside of test beams. An implementation of this with the Lund Telescope and some of the associated first results is then presented in chapters 6 and 7.

4 Sensor characterization in a particle beam

The most common way to characterize and study pixel sensors is using a particle beam. During the Engineering Run 1 (ER1), the MOSS (as well as babyMOSS) sensors have been extensively studied in various test beam campaigns starting from April 2023 up to September 2025. The studies involved both testing of irradiated and non-irradiated chips in order to determine the performance of the pixel matrix under ITS3 operating conditions [34]. The following chapter details the latest test beam that took place in September of 2025, at the Proton Synchrotron (PS) at CERN.

PS is a particle accelerator located at CERN's East Area, which is in operation since the early 1960s [39]. It hosts 4 secondary beamlines: T08, T09, T10 and T11, that provide different maximum beam momentum. September's test beam took place at the T10 beam line, that delivers secondary particles up to 7 GeV/c and can reach $p_{max} = 11.5$ GeV/c [40].

The non-irradiated babyMOSS sensors were tested using a 7 GeV/c negative pion beam. The two main measurements focused on sensor detection efficiency and spatial resolution. Two different devices under test (DUTs) of different splits were tested: babyMOSS-2_5_W06D0 (split 1) and babyMOSS-2_1_W21D4 (split 2). Only the region 0 of top and bottom HUs were enabled for both DUTs.

The following chapter presents the telescope set-up, triggering scheme and sensor configurations.

4.1 Telescope set-up

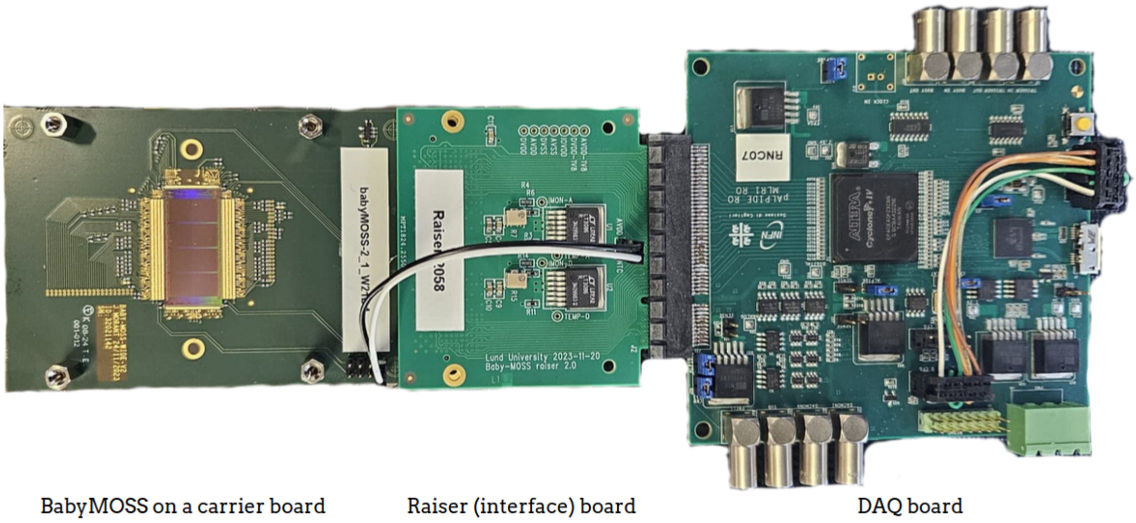

Figure 14: Layout of the babyMOSS telescope plane.

The main components of the telescope are the babyMOSS planes, where a babyMOSS sensor, mounted on a carrier card, is connected through an interface board, called Raiser board, to a DAQ board, as is shown in Figure 14. Figure 15 shows the telescope set-up used in the test beam. In the set-up, 6 such planes were used as tracking planes, 1 was used as a DUT, and it was placed in the middle of the tracking planes. The set-up also contained 2 scintillators, one placed before the first tracking plane, and one placed after the last. The scintillators were positioned in a way to only overlap over the region 0 of the top and bottom HUs, as is shown in Figure 16: the front scintillator covers only the region 0 and the back scintillator covers the whole sensor matrix. This increases the trigger efficiency, as the trigger cycle is initiated only when particles pass region 0. The distance between the tracking planes is 25 mm and the distance from the tracking plane to the DUT is 37 mm on both sides of the DUT.

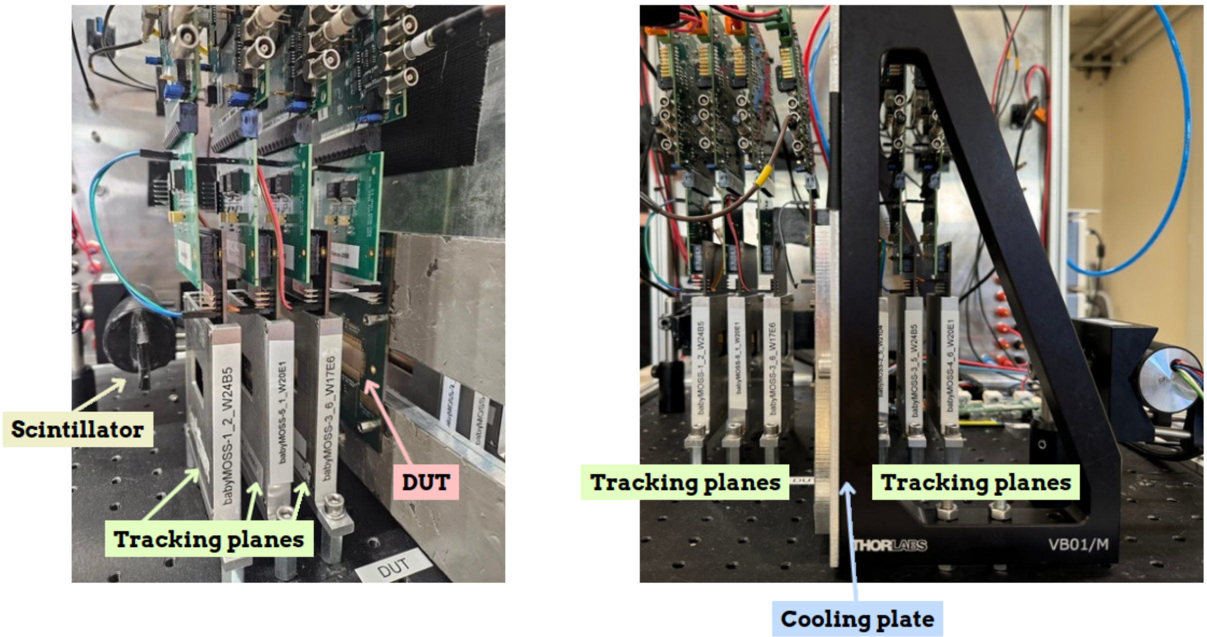

Figure 15: Layout of the telescope used in the test beam of September 2025. In the image on the left, the DUT can be seen mounted on a cooling plate and in the image on the right the full telescope set-up is visible.

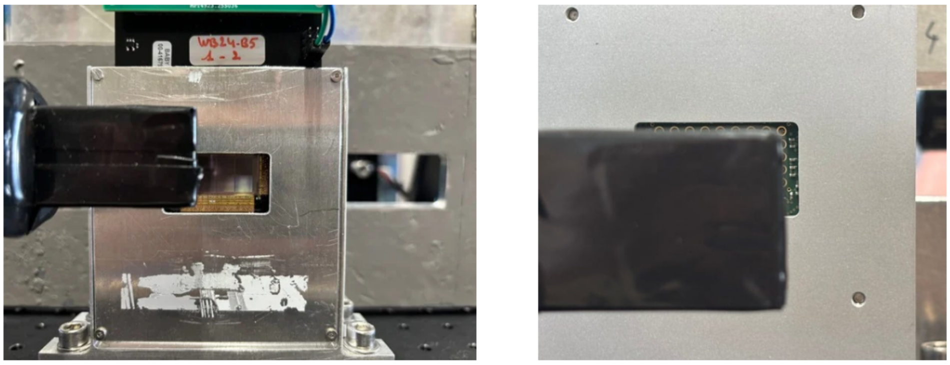

Figure 16: The positioning of the front scintillator (left) and the back scintillator (right), so that they only overlap on the region 0 of both HUs.

The DUT was mounted on a cooling plate, as can be seen in Figure 15. The water-cooled plate helped maintain a constant 27°C temperature during the entirety of the test beam. In addition, it allowed to study the sensors at the expected operational conditions for the ITS3 [34].

In addition, a reverse bias (known as P_{sub}) of -1.2 V was applied through the set-up in order to maximise the depletion region of each of the pixel. P_{sub} essentially maximises the region where a particle can be detected, making the detector more efficient.

4.2 Triggering scheme

The telescope operates in the triggered readout mode. When a particle passes 2 scintillators, the read out sequence is initiated in the telescope: the trigger signal is propagated through the tracking planes until it reaches the DUT. Then each DAQ board asserts its own busy signal and the longest one reaches the trigger board, as is represented in Figure 17.

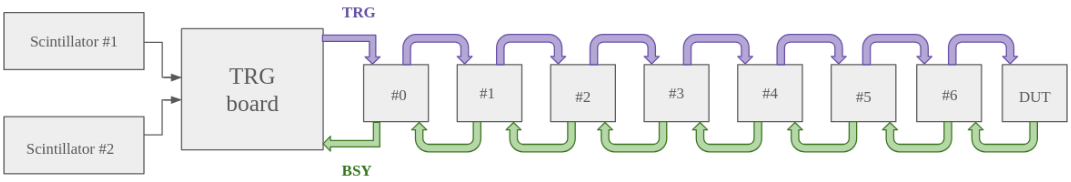

Figure 17: Triggering scheme used in the test beam.

The trigger board's logic is configured as follows:

```
TRG0 & TRG3 & trg_dead_time> 10000 & dt_veto > 5000 & !BSY
```

TRG0 and TRG3 are the trigger inputs, corresponding to the channels 1 and 4 of the trigger board, to which the 2 scintillators are connected. The board is configured with the *AND* logic gate between CH1 and CH4, meaning that when a particle passes both scintillators in coincidence, the triggering sequence is initiated. `trg_dead_time` corresponds to a fixed dead time of the trigger board, which defines the distance to the previously issued trigger signal. The time is set to internal clock cycles (CC). For the trigger board used in the test beam 1 CC corresponds to 10 ns, so the dead time of the trigger board is set to 1 µs. `dt_veto` represents the 'veto' time that is added to the trigger boards dead time (in this case, 50 µs) every time a new particle hits both scintillators. The combination of the two last parameters helps to ensure that the DUT receives and processes only one signal at a time. Lastly `!BSY` indicates that a trigger sequence can be started only when the busy signal is de-asserted.

In addition to these parameters, the strobe length, which corresponds to a window of time for which a sensor is active for particle hits, was set to 200 CC, which corresponds to 6 µs (internal clock cycle of the DAQ board is 1 CC = 30 ns).

The logic of the trigger board is configured using *AND* operators. If all of the above conditions are satisfied, the trigger signal, to start a readout cycle is sent to the telescope planes. However, if any of the conditions return false, no new trigger signals are sent into the system.

4.3 Threshold tuning

The physical threshold value per region is controlled by an internal voltage called V_{casb}. In order to achieve the most optimal operating conditions of the telescope, threshold tuning had to be performed for both the tracking planes and the DUTs. This involves running fake-hit rate (FHR) and threshold (THR) scans for region 0 of top and bottom HUs [34]:

- **Fake-hit rate scan**: helps determine the number of fake hits due to noise within a region. During a FHR scan, thousands of triggers are sent to the sensor, in absence of particles or any charge injections, and number of hits per pixel are recorded. Pixels that register a hit in more than 1% of issued triggers are classified as noisy and can be further masked to reduce the noise in the region.

- **Threshold scan**: helps assessing the detector's performance and to determine the threshold of the sensor for a specific configuration. During a THR scan, various charges are injected into the sensor by performing pulsing of the injection capacitor in each pixel. Then, the response of each pixel is tracked for an increasing amplitude of injection charge.

Firstly, FHR and THR scans were performed for the 6 tracking planes, to determine the threshold values that minimise noise in each of the planes. Since these planes are used only for track reconstruction purposes, the threshold was set to relatively low, 15 DAC units [2] for all tracking plane region 0 of both

[2] The threshold is set internally using DAC units. They can be converted to number of electrons by performing calibration on each of the sensors, using their internal pulsing. Such calibrations were only performed on the DUTs and not on the tracking planes.

HU, which allows to keep FHR low (less than 10^{-8} hits/pixel/event) and tracking efficiency high (more than 95%). The same scans were performed for the 4 DUT candidates, out of which 2 were chosen as having the lowest fake-hit rate levels within region 0.

A V_{casb} range finder was used in order to determine the range of possible threshold values for each of the region 0 of the two DUTs. The script performs both FHR and THR scans for a range of V_{casb} values, in order to identify the maximum V_{casb} to be used for data taking. This corresponds to the lowest threshold value for which the FHR level is 10^{-3} hits/pixel/event. Having this, it was then possible to define 10 V_{casb} values, decreasing from the highest in steps of 3 DAC, used for data taking.

4.4 Data taking and analysis configurations

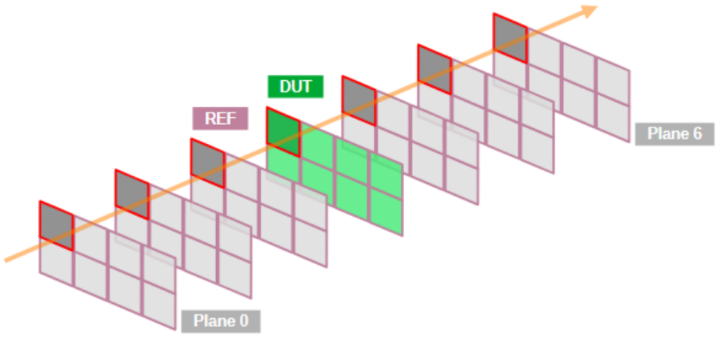

Figure 18: Schematic showing the beam passing through region 0 of the top HU in all of the planes, due to the beam being perpendicular to the telescope.

The telescope, placed on a moving table, was aligned so that the beam focused on region 0. In addition, the beam was perpendicular to the telescope set-up, as is shown in the Figure 18.

For data acquisition, EUDAQ2 framework [41] was used. Dedicated initialization and configuration files, detailing the parameters of the set-up were necessary. In particular, for the detection efficiency measurement, 10 separate configuration files had to be created for each DUT, each having a different threshold value for the region 0 of top and bottom HUs.

For data analysis, Corryvreckan framework [42] was used. It is a modular software, requiring geometry and configuration files in order to understand the set-up of the telescope and reconstruct events, loaded from EUDAQ2-type raw files. Corryvreckan performs noisy pixel masking, telescope alignment in 3 steps (pre-alignment → alignment without DUT → alignment with DUT) and also data analysis. For the alignment step, the *AlignmentMillepede* algorithm is used, that allows a simultaneous fit of both the tracks and the alignment constants [43]. After alignment, the set-up geometry file is updated with more exact plane positions and orientations in the xyz-plane.

It is noted here that the existing software implementation treats every region of a babyMOSS sensor as a separate plane (a sensor is therefore divided into 8 regions). Thus, an event is only selected for tracking if a particle has left a hit in the same region and HU of all 6 tracking planes.

For analysis, the most relevant modules with specified parameters are detailed in the following [43]:

- *Tracking4D* module reconstructs the tracks using the general broken lines fit, that takes material budget and scattering into account. In this case, DUT is excluded and clusters of different tracking planes are associated if they fall within a 500 µm radius circle.

- *DUTAssociation* module allows forming an association between clusters on the DUT plane and the reference track.

- *AnalysisDUT* module generates a number of plots that can be used to estimate detectors performance, of which the most important here are the 1D histograms of track residuals and correlations for different cluster sizes. The module allows rejecting tracks based on their χ^2/ndf value, which for the analysis was set to 3. Examples of χ^2/ndf and residual plots for the babyMOSS-2_5_W06D0 sensor can be found in Appendix A.

- *AnalysisEfficiency* module gives the detection efficiency with its uncertainties. The measurement is obtained by comparing the cluster positions of the DUT with the interpolated track position at the DUT. For this module the telescope tracks were accepted only if $\chi^2/\text{ndf} < 3$.

4.5 Hit maps and Correlations

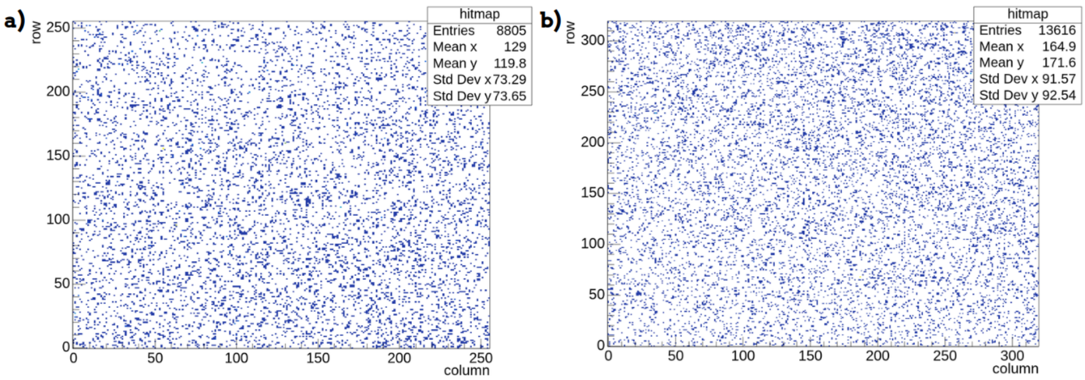

Figure 19: DUT hit maps of the a) region 0 of the top HU and b) region 0 of the bottom HU.

Figure 19 shows the hit maps of the region 0 of a) top and b) bottom (right) HUs of one of the DUTs (babyMOSS-2_5_W06D0), obtained using the negative pion beam. The hits correspond to all data points that were recorded during a single run and then, using the event converter, displayed by Corryvreckan. Each region of one babyMOSS sensor is treated as a separate plane, therefore the results for region 0 of top and bottom HU appear on separate plots.

In addition, Corryvreckan also provides spatial correlation plots in x and y coordinates, which can give a rough idea on how well the sensor planes are aligned. Figure 20 shows row/row (or y/y) coordinate correlations for the bottom HU of different planes. Figure 20 b) corresponds to the third tracking plane, which was set as a reference plane in the geometry configurations for Corryvreckan. This means that during alignment steps, the position of this plane is fixed, and the positions of other planes get adjusted accordingly. Because of this, the correlation plot shows a thin diagonal line, centred at 0. Figure 19 a) shows the first tracking plane. The diagonal is centred at 0, meaning that the two planes are well aligned in the y direction. For the DUT, (Figure 19 c)), there is a slight offset from 0. This indicates that there is a slight misalignment between the two planes. This misalignment is accounted for in the third step (alignment with DUT) of Corryvreckan alignment process. Figure 19 d) shows the row/row correlation plot for the last tracking plane, located the furthest from the reference plane. The diagonal has a wide spread, which is due to multiple scattering and also can indicate a slight rotational misalignment between the two planes. Correlation plots for other planes and for the top HU can be found in Appendix B.

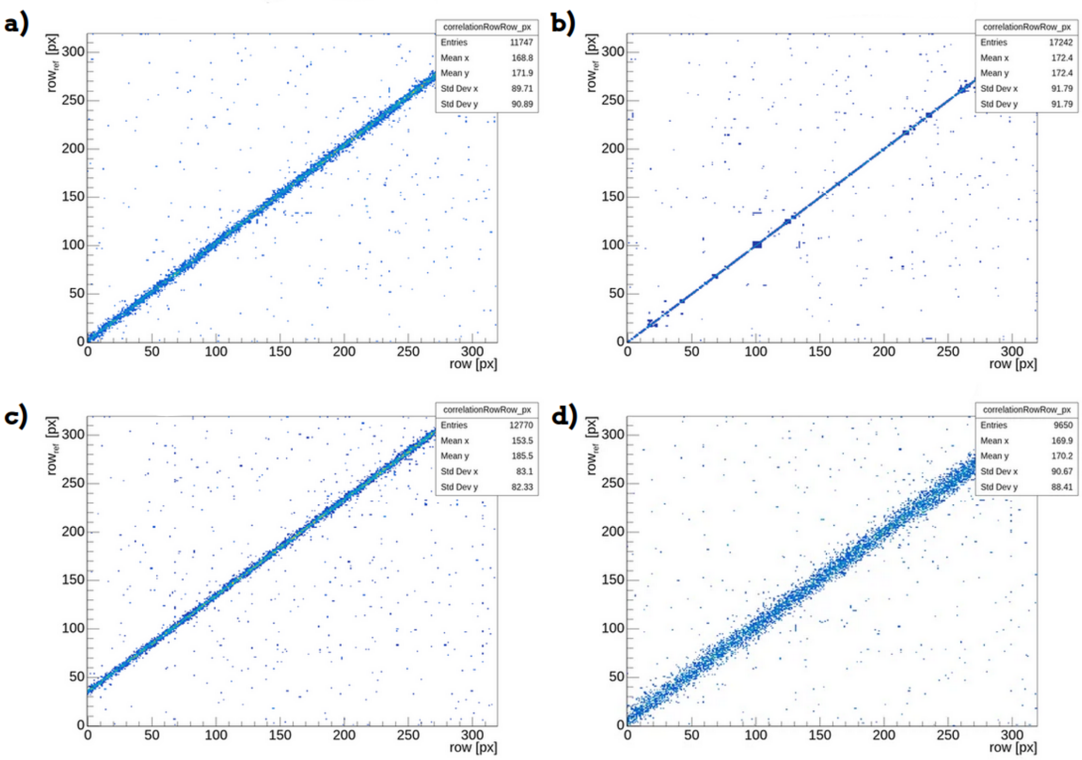

Figure 20: Row/row correlations for bottom HU of different planes: a) first tracking plane (plane 0), b) third tracking plane (plane 2), also set as a reference in Corryvreckan geometry files, c) DUT plane (plane 3) and d) last tracking plane (plane 6).

5 Test beam results

In this section, the main results of the September 2025 test beam of the detection efficiency, fake-hit rate, spatial resolution and cluster size are presented. The data was taken using a babyMOSS beam telescope with a beam of 7 GeV/c negative pions. The comparison is made within the same sensor between the two HUs of different pitch and between the two DUTs of different splits.

5.1 Detection efficiency

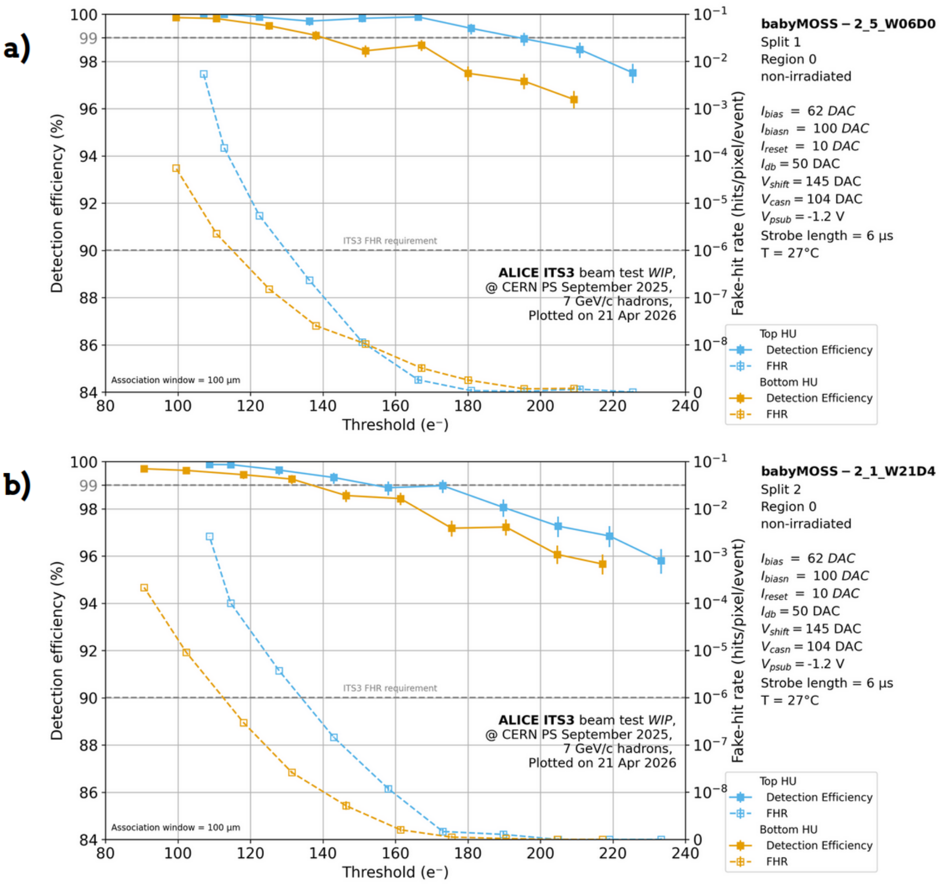

Figure 21: Detection efficiency and fake-hit rate as a function of the threshold for a) babyMOSS-2_5_W06D0, of split 1, and b) babyMOSS-2_1_W21D4, sensor of split 2. Results are shown for the region 0 of top and bottom HUs.

Figure 21 shows the detection efficiency and fake-hit rate plots as a function of the threshold for the two different DUTs. Figure 21 a) shows the results for the sensor of split 1 and Figure 21 b) corresponds to the sensor of split 2. Solid line represents the detection efficiency (percentage) in terms of the threshold (in electrons) and the dashed line represents the fake-hit rate (hits/pixel/event) in terms of the threshold. The different colours correspond to the top (blue) and bottom (orange) half units that have different pixel sizes. For the ITS3 upgrade, it is required for the detection efficiency to be higher than 99% and for the fake-hit rate to be lower than 10^{-6} hits/pixel/event [5] (these values are also represented in the plot with a gray dashed line). This defines an operational margin for both of the sensors where they have the best performance. For the detector of split 1, the range of the operational margin is around 65 e^- for the top HU and around 25 e^- for the bottom HU. For the detector of split 2 it is around 40 e^- for the top HU and 30 e^- for the bottom HU.

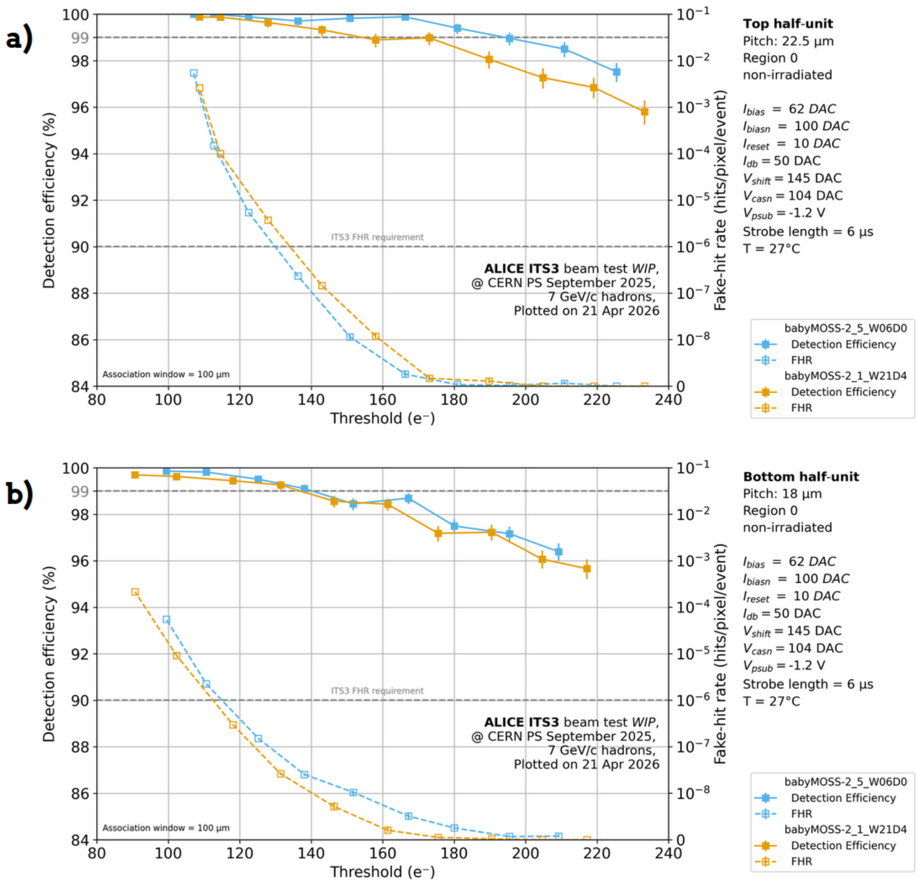

Figure 22: Detection efficiency and fake-hit rate as a function of the threshold for a) top half-units and b) bottom half-units. Results are shown for two sensors of different splits.

The plots show a better detection efficiency for the top HU for both sensors. It can be concluded, that detection efficiency is better for a larger pixel pitch. These results are consistent between the two sensors of different geometry and are also consistent with measurements done in previous test beams [34]. It can be explained by the fact that for sensors of a smaller pitch size, a particle is more likely to hit on, or close to, the borders of the pixel and, due to charge sharing of neighbouring pixels, go below the threshold value and be undetected by the sensor. The opposite is true for sensors of a larger pixel pitch size.

A further comparison can be made for the two HUs of sensors of different splits. Figure 22 shows the plots for the top HU (a) and of the bottom HU (b) of the two sensors. The bottom HU has the exact same geometry in both cases: pixel pitch of 18 µm and gap size of 2.5 µm, therefore the detection efficiency for this HU is comparable between the two sensors of different splits, as can be seen in Figure 22 b). Top HU has the same 22.5 µm pixel size in both sensors, however the main difference is the gap size: split 1 sensor (in blue) has a gap size of 2.5 µm and and the split 2 sensor (in orange) has a gap size of 5 µm in between the pixels. It can be concluded from the Figure 22 a) that the pixel matrix, having a smaller gap between the pixels shows a better detection efficiency. This comes from the fact that for this type of geometry, the electric field at the pixel border is larger than for a geometry with a larger gap. This minimises charge sharing and in turn, increases the detection efficiency. Fake-hit rate shows no significant difference between the two geometries. These results are consistent with analysis results from previous test beams [34].

5.2 Spatial resolution

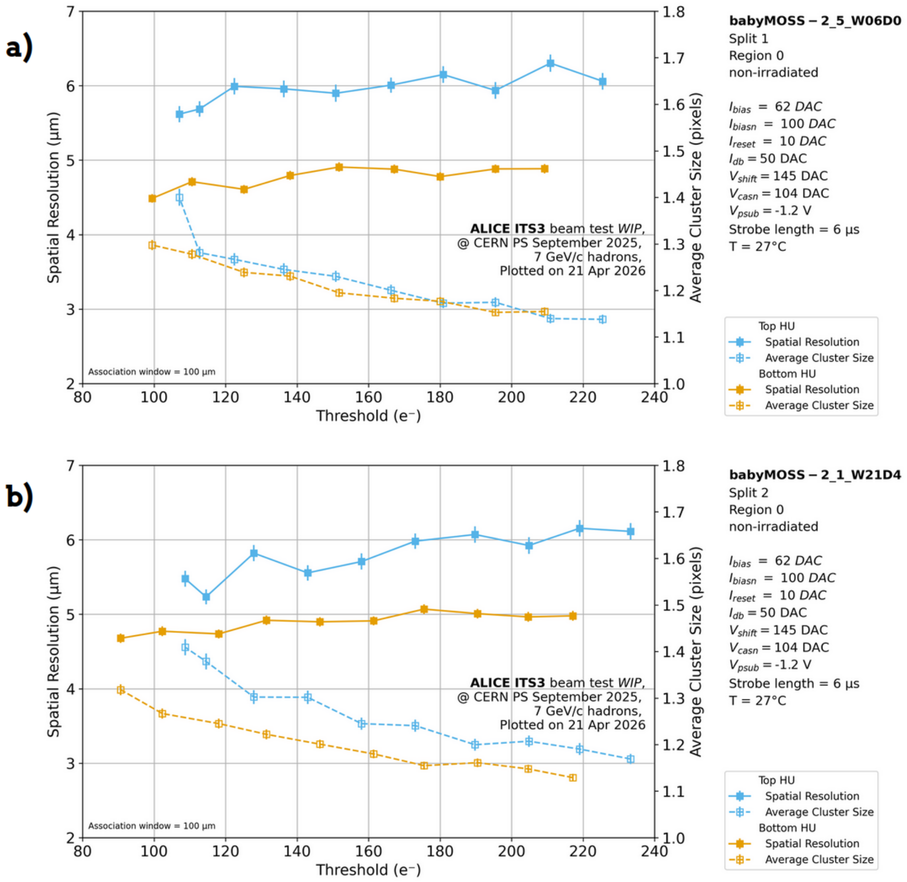

Figure 23: Spatial resolution and average cluster size as a function of the threshold for a) babyMOSS-2_5_W06D0, of split 1, and b) babyMOSS-2_1_W21D4, sensor of split 2. Results are shown for the region 0 of top and bottom HUs.

Analysis to determine the spatial resolution (in µm) and average cluster size (in pixels) as functions of the threshold (in electrons) were also performed. Figure 23 shows the results for the two different DUTs and Figure 24 shows the results for the HUs.

From the Figure 23 it is clear that for both sensors, the bottom HU has a better spatial resolution, of around 4.5-4.9 µm, than the top HU, of around 6 µm: the spatial resolution is better for a smaller pixel pitch. Both values are better than the binary resolution[3], corresponding to ~ 6.5 µm for top HU and to ~ 5.2 µm for bottom HU. This is due to the fact that the average cluster size for both HUs is larger than 1. Additionally, the plots also show that for an increasing threshold, the spatial resolution gets worse and the average cluster size decreases. The target spatial resolution for the ITS3 upgrade is of 5 µm. For both sensors, this resolution is achieved only by the bottom HU.

Figure 24 compares the spatial resolution and average cluster sizes for the same HUs of the two sensors. For the top half unit, the split 1 sensor (blue) that has a smaller gap size has a slightly worse spatial resolution and a smaller average cluster size, while the opposite is true for split 2 sensor (orange), whose gap size is twice as big. This is because for a larger gap size, the average cluster size is larger, resulting in a better spatial resolution.

As for the bottom HUs, both sensors have the exact same geometry and therefore both results are

[3]Binary resolution is the theoretical best spatial resolution that can be achieved, assuming there is no charge sharing. It is calculated by $\sigma = p/\sqrt{12}$, where p is pixel pitch.

comparable. Overall it can be observed that the HUs with a smaller pitch size have a better spatial resolution. This agrees with the results from previous analyses [34].

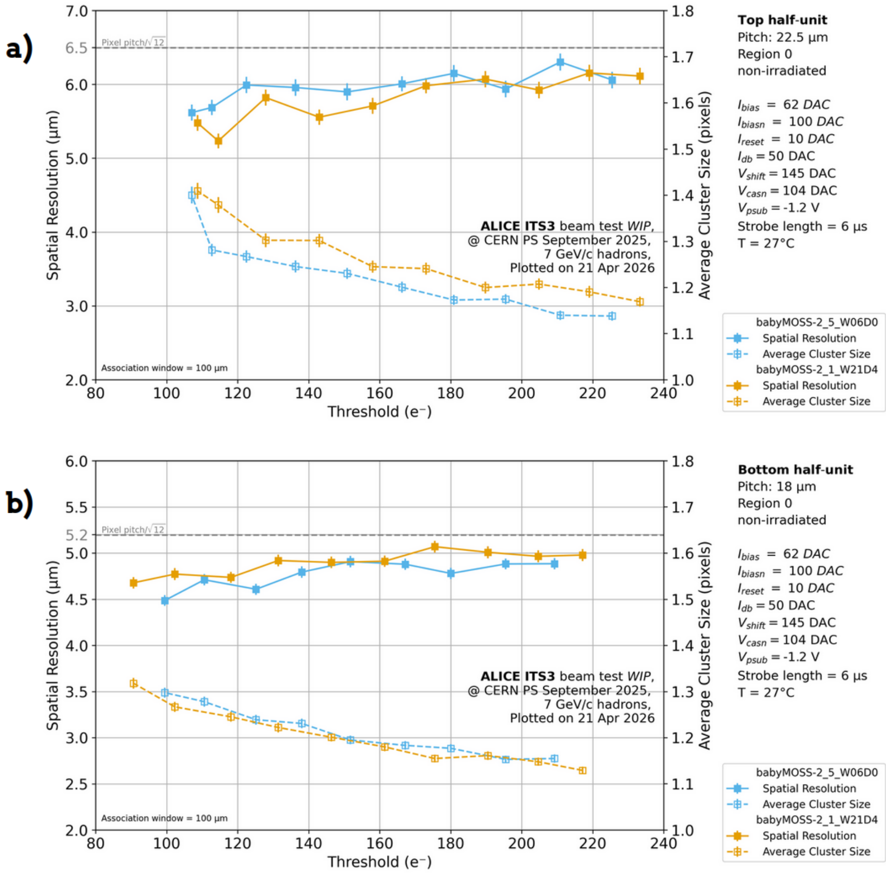

Figure 24: Spatial Resolution and average cluster size as a function of the threshold for a) top half-units and b) bottom half-units. Results are shown for two sensors of different splits.

6 Development of the Lund Telescope

Due to the upcoming LHC Long Shutdown 3, there is going to be no beam available at the PS, from end of August of 2026. For this reason, a compact muon telescope has been built at the Lund Physics department. It will allow to study the detection efficiency, dead areas and pixel response uniformity of the babyMOSS sensors. In addition, it will be possible to study future prototypes in-house, without having to plan for a test beam.

This chapter mainly covers cosmic muon sources, the set-up of the telescope, the software implementations and threshold tuning.

6.1 Cosmic muon sources

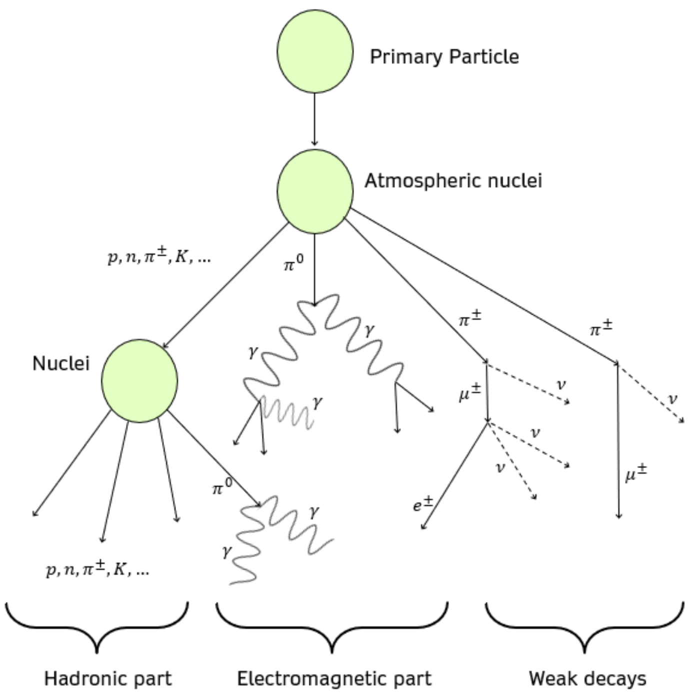

Figure 25: Extensive Air Shower (EAS) - graphic visualization.

Muons are second generation particles, belonging to the lepton family, of mass $m_\mu = 105.66$ MeV/c^2, and lifetime 2.2 µs [6]. Sources of atmospheric muons are known as Extensive Air Showers (EAS), coming from high-energy cosmic radiation, shown also in Figure 25. EAS starts when an extremely energetic cosmic particle interacts with the atomic nuclei of the atmosphere via the strong interaction. This results in the production of secondary particles, the most abundant of which are pions (π^0, π^+, π^-) [44]. Neutral pions then decay into 2 photons, producing electromagnetic showers, also known as photon, electron and positron cascades [8]. Charged pions primarily decay into muon-neutrino pairs, constituting the hard component of the shower, due to their ability to easily penetrate the atmosphere.

$$\pi^0 \rightarrow \gamma + \gamma$$

$$\pi^+ \rightarrow \mu^+ + \nu_\mu$$

$$\pi^- \rightarrow \mu^- + \bar{\nu}_\mu$$

Muons, in particular the ones that have low energy, can eventually decay into electrons and neutrinos, contributing to the soft component of EAS [6].

$$\mu^+ \rightarrow e^+ + \nu_e + \bar{\nu}_\mu$$

$$\mu^- \rightarrow e^- + \nu_\mu + \bar{\nu}_e$$

While neutrinos, only interacting trough the weak interaction, are extremely difficult to detect, cosmic muons, having energy which is larger than a few GeV, have a very high probability of reaching the earth and being detected [8, 45]. The continuous source of ionizing particles allow for year-round data acquisition and sensor characterization. Because of this, muons provide an appealing alternative to test beams.

6.2 Lund Telescope set-up

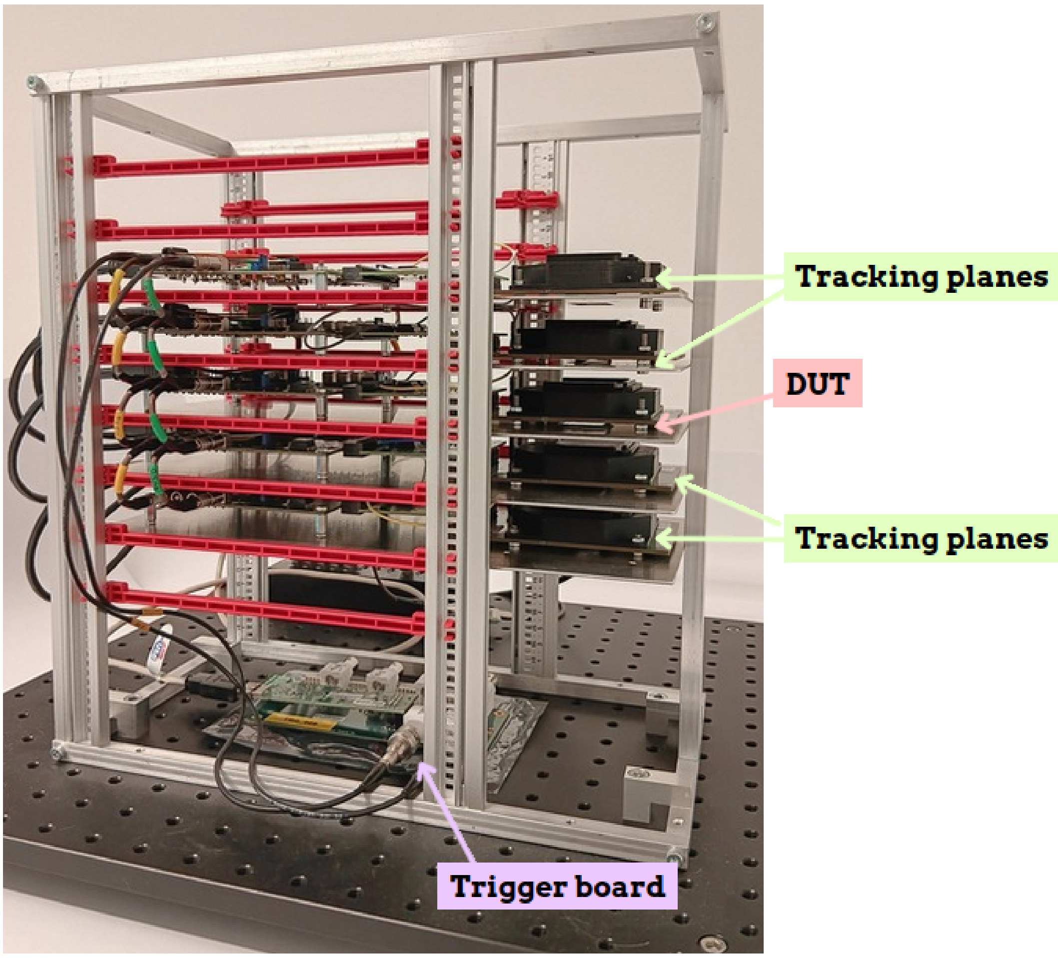

Figure 26: Compact Lund Cosmic Telescope.

The Lund Telescope is shown in the Figure 26. It is made up of 5 babyMOSS planes, where a single plane comprises a babyMOSS sensor, a Raiser board and a DAQ board, as was used in the test beam of September 2025 (see also Figure 14). The middle plane was used as the DUT, while the 4 other planes were used as tracking planes. The babyMOSS planes are spaced 3 cm from one another and this compact configuration allows to achieve tracking resolution of 3.51 µm for the top HU and 2.91 µm for the bottom HU. Considering that the babyMOSS sensor active area is ~ 3.6 mm^2 (1.4 cm $\times$ 2.59 cm), the spacings in between the sensors reduce the angular acceptance of the telescope. For muon tracks passing through all 5 sensor planes, the angular acceptance is ± 6° in x and ± 12.2° in y. Seen also in the Figure 26 are the frame, metal plates on which the planes rest, and babyMOSS covers, that were all custom made in Lund University.

The babyMOSS cosmics telescope is similar in many ways to a beam telescope, described in chapter 4. However there are some differences, the most important being the fact that the Lund Telescope does not use scintillators for triggering, unlike the babyMOSS telescope used in the test beam. Trigger signal in this case is generated by the trigger board, whose functioning is described in detail in the next section.

6.3 Triggering scheme

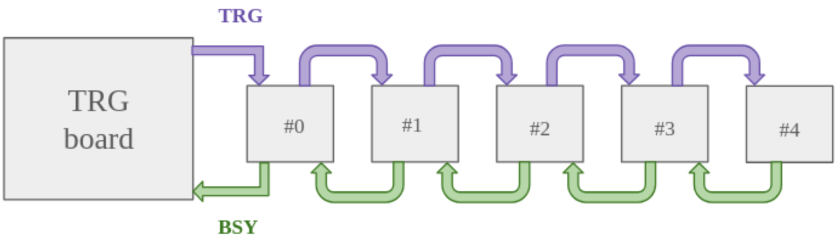

Figure 27: Triggering scheme used for the Lund Telescope.

The triggering scheme used for the Lund Telescope functions in a continuous acquisition mode. Graphic representation of the triggering scheme used is shown in Figure 27. The trigger board generates a trigger signal that propagates through the DAQ boards from the top plane (noted in Figure 27 as #0) to the bottom plane (noted in Figure 27 as #4). Busy signal is also asserted in all of the DAQ boards. The FPGA of the trigger board uses the following logic to output the trigger signal to start the data acquisition cycle:

```
trg_dead_time > 20000 & !BSY
```

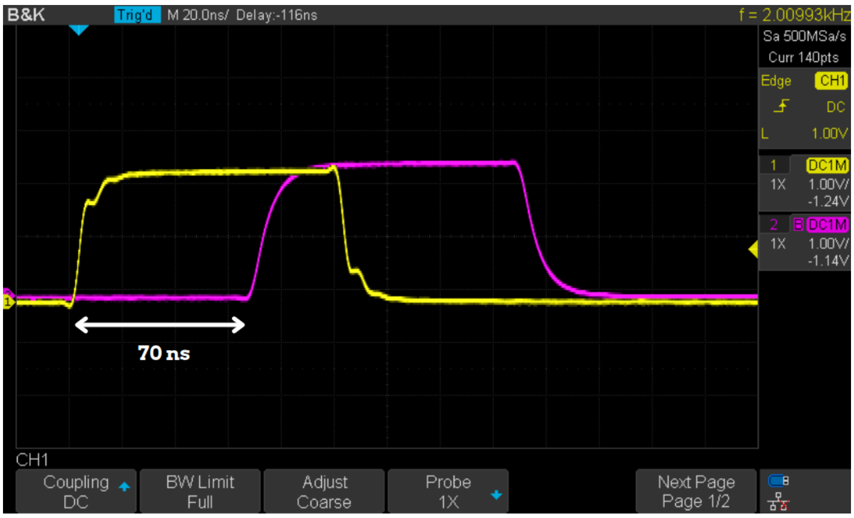

Figure 28: Oscillogram showing the trigger signal in the first plane (yellow) and the last plane (pink). The total propagation delay of the trigger signal from the first to the last telescope plane is 70 ns.

Because the muon flux at sea level is 1 muon/cm^2/min, in order to have an efficient muon telescope, sensors have to be active for data acquisition the maximum amount of time possible. To achieve this, parameters of the triggering scheme have been optimized with the help of an oscilloscope. The strobe

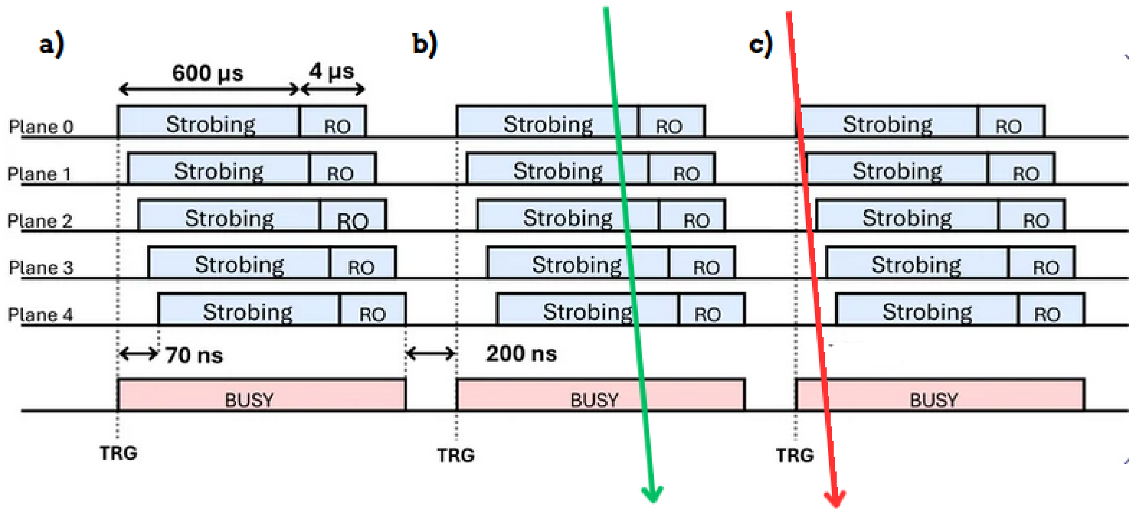

Figure 29: Data acquisition sequence with the discussed triggering scheme of the Lund Telescope, where a) shows the settings chosen for the telescope, with the delays between the strobe windows of each plane; b) shows an event where a particle has passed the telescope during the strobing window of all 5 planes and c) shows a particle passing the telescope only during the strobing window of the first two planes - in the case where at least 3 planes with hit are required, this event will not be recorded, unless the charge deposited is sufficient enough to maintain the signal over the threshold for long enough, so that the strobing window starts in other planes.

length, or the time window for which the chip is sensitive to hits, chosen for each of the sensors is 20000 CC, which corresponds to 600 μs. The readout, or the time it takes for the babyMOSS sensor to send the data to the FPGA of the DAQ board is approximately 4 μs. It has been determined using the oscilloscope that there is a $10-20$ ns delay between the start of the strobing window in-between the sensors, meaning that when the strobing starts in the first sensor, it takes about 70 ns for the strobing to start in the last sensor, as can be seen in Figure 28 (here first sensor refers to the uppermost plane and last sensor refers to the lowermost plane). The blind time of the sensors themselves, is about 200 ns, which corresponds also to the distance between two consecutive trigger cycles (in the case where all trigger scheme settings are described as above).

Due to this propagation delay, there are three possible cases when a particle passes the telescope:

1. If a muon arrives within the strobing window of all planes, it will be detected in all sensors. This is the situation shown in Figure 29 b).

2. If a muon arrives when plane 0 and plane 1 have started the strobing window, but it has not yet started in other planes, as is shown in Figure 29 c). If a muon will be detected in all 5 planes, will depend on the amount of charge deposited. If enough charge is deposited, and the time the signal is over the threshold is long enough for the strobing to start in all 5 planes, the particle will be detected in all sensors.

3. If a muon arrives when the strobing window has ended in at least 3 of the planes, the muon will not be detected.

Overall, having a triggering scheme, functioning in a continuous data acquisition mode, and with optimized strobe length values of 600 μs, the Lund Telescope has an active duty time of 99%.

6.4 Software development

For data acquisition, the EUDAQ2 ITS3 modules, developed for the beam telescope, cannot be used, as they are not optimized for the use case of Lund Telescope. In order to make continuous data acquisi-

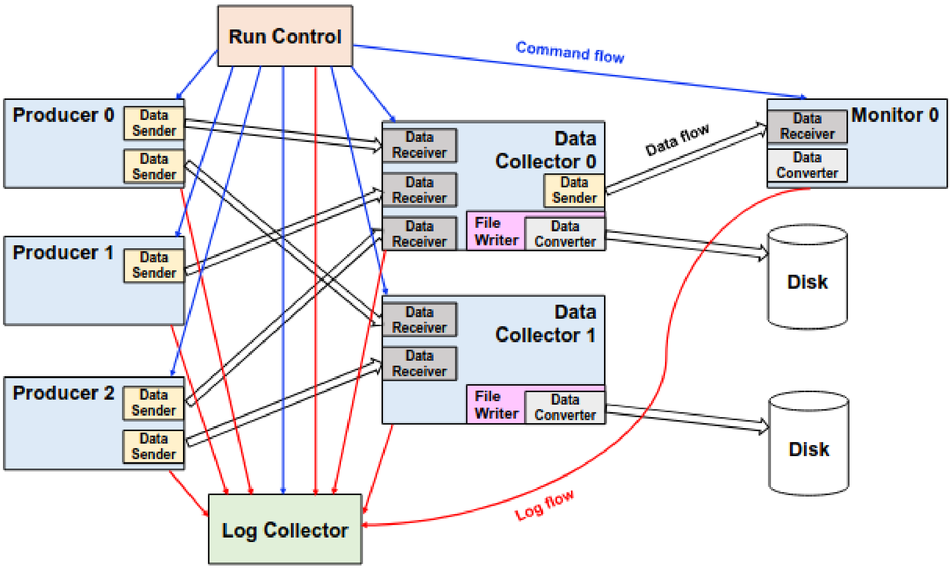

Figure 30: Architecture of EUDAQ2 framework. Sourced from [47].

tion, without a trigger coming from a particle, work, extensive software developments were carried out. Implemented features cover the telescope plane control and readout, data collection, event building, and event conversion.

EUDAQ2 software [41] is a data acquisition framework, written in C++. It is modular and flexible, originally designed for EUDET-type pixel beam telescopes, but now used for operating different detector prototypes at test beams at different accelerator facilities [46].

The software's architecture is shown in Figure 30. EUDAQ2 is split into different processes, such as Run Control, Producer, Data Collector, Log Collector, Online Monitor, etc. They communicate with each other via TCP/IP sockets [47]. A central Run Control manages the whole system by sending out commands to other processes and by receiving status reports from them, as is represented by the arrows in Figure 30. A typical data acquisition run is started with dedicated initialisation and configuration files, that are analysed by the Run Control. The dedicated information is then sent out to other EUDAQ2 processes.

A EUDAQ2 Producer module is responsible for controlling the underlying detector hardware by performing initialization, configuration, stopping and starting. Each detector in a telescope requires its own Producer instance, that all run in parallel. A Producer also reads out data and sends it to the Data Collector, which gathers and merges raw data from all of the Producer instances, and then writes it to file. An important process in every run is the Log Collector. It is in charge of receiving, logging and writing to file log and error messages from other EUDAQ2 processes, which helps with debugging.

Additionally EUDAQ2 provides a Monitor functionality, that reads the raw data file and generates different plots for display, such as hit maps and cluster maps for each of the detectors participating in a run, correlation plots, hit per events and hit per plane plots.

For the Lund Telescope, user-specific implementations of different processes were necessary. The main developments were done for the Producer and Data Collector processes, event selection was implemented to account for the continuous trigger scheme. Moreover, a dedicated event converter had to be implemented, to combine the different regions of one sensor. These are discussed in the sections below.

6.4.1 BabyMOSS Producer

The Producer in the EUDAQ2 framework is a core module that implements an interface to the underlying detector hardware. By reading information from the initialisation and configuration files, each producer sets up the babyMOSS plane for operation and controls the data acquisition process for each plane.

For the purposes of the Lund Telescope, the following functionalities, not present in previous Producer implementations for the babyMOSS sensor, were added:

- The possibility to set the trigger mode of the babyMOSS plane to either 'replica' or 'primary'. The latter type allows the plane to receive trigger signals from the software periodically and then propagate them to the rest of the set-up, that consists of type 'replica' planes. This implementation was added to allow for software generated triggers, without having a trigger board in the set up.
- The possibility to define a number of noisy pixels in the initialisation file and add specific tags to events, depending if they have less or more hits than the number of noisy pixels for a particular plane. In general, events that have more hits than the number of pixels in a plane, get a "Hit" tag assigned to them.
- The possibility of providing a mask file, containing the coordinates (HU, region, row, column) of noisy pixels and masking them directly on-chip. The coordinates of these pixels will never appear in the raw data packets as they are ignored by the software.
- Periodic temperature monitoring.
- The possibility to perform time over threshold measurements.

6.4.2 Trigger board Producer

Trigger board is another piece of hardware that requires its own Producer, to act as an interface to control the underlying trigger board hardware. The Producer sends trigger configurations to the FPGA of the DAQ boards, starts the trigger sequence, once all planes are configured. An additional functionality was added to periodically stop sending triggers, in order to allow all babyMOSS Producers to perform status checks for currents, voltages and temperatures.

6.4.3 Event Selection

One of the functionalities of the Producer is reading out data and sending it to the Data Collector, which gathers and merges raw data from all of the Producer instances, and then writes it to a file. Each time read out occurs, there is data sent out from the sensors, to the computer. This includes all hit events, noise and empty events, in the case where no hits were recorded.

According to MOSS data protocol, the minimum amount of space required to encode an event is 8 bytes [35]. This corresponds to an empty data packet (when no hits are recorded) that is represented as a byte sequence. On top of that, a single hit, whether noise or a particle hit, is encoded using 3 bytes, that represent the row and column of the pixel where that hit has occurred. Due to the nature of continuous data acquisition, implemented for the use case of Lund Telescope to detect muons, the data coming from each of the planes is constantly being written to file by the Data Collector. If data was saved every trigger cycle, the raw data file sizes would increase by 13 kB every second, assuming only empty events are recorded, an no noise is present in the pixels. This quickly increases the size of the raw data files, which becomes a problem, especially for long-term data taking periods of up to several months. To counteract this, data management routines had been introduced in both Producer and Data Collector processes. The following is implemented:

- Noisy pixels are masked directly in the Producer.
- All non-empty events get a "Hit" tag assigned to them by the Producer. All of the data then gets sent to the Data Collector.

- In the configuration file, minimum number of planes with hit is defined. Data Collector will only build a telescope event if the number of planes with hit is equal or higher than the defined minimum.
- Data Collector periodically checks how many raw events with a ”Hit” tag were sent by each Producer. If the number of ”Hit” events from each of the planes corresponds to the required minimum planes hit, a telescope event is built, a timestamp to this event is added and it is written to the raw file.

Figure 31 shows the average number of hits per event, per plane (it should be noted here that planes here are further divided into two HUs: tb_plane for the top HU and bb_plane for the bottom HU). For each of the planes, the average number is below one, meaning that the events recorded do not contain noise. If noisy pixels were not masked, average number of hits would increase to above 1 (the value would depend on how many noisy pixels are present on a given plane), because the noisy pixels would produce data at every trigger cycle. Furthermore, due to the fact that an event is built only in the case where at least 3 planes have events with ”Hit” tag, the middle plane (in the Figure 31 marked as tb_plane 4 and bb_plane 5, belonging to the babyMOSS-3_2_W05D5 of the Lund Telescope) has the highest number of hits per event.

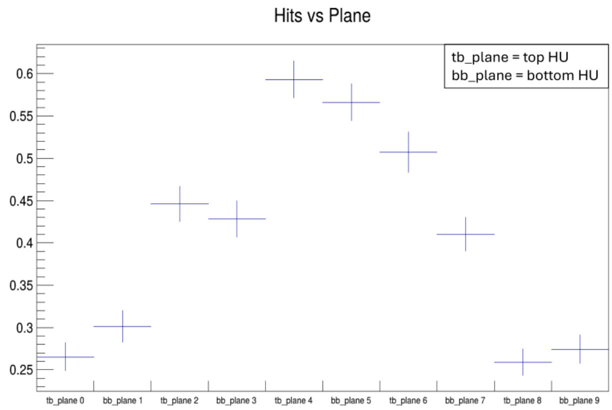

Figure 31: Average number of hits per event (per plane), taken from the Lund Telescope commissioning run data.

6.4.4 Event Converter

Event Converter is a EUDAQ2 process, that does not directly participate in the data taking, but is rather used to convert the raw events into standard events. A standard event can be then used as input data for any non-EUDAQ2, data analysis software [47], for example, by the Corryvreckan framework [42].

Contrary to the test beam situation, the muons will enter the particle telescope at various angles and will leave non-perpendicular tracks. In its pre-existing Event Converter process, the babyMOSS sensor had 8 output planes, one for each of the regions in the top and bottom HUs. This means that during the event conversion, each of the regions within one babyMOSS plane is treated as a separate sensor and only the particles that have crossed the exact same region in all of the tracking planes can be used for track reconstruction and data analysis. For the Lund Telescope, this process was modified to output 2 planes instead: one for the top and another for the bottom HUs. This way, inter-regional hits within one half unit can be analysed, which significantly increases the statistics.

Figure 32 shows an example of a hit map for two HUs of one babyMOSS sensor. Contrary to a hit map from the test beam shown in Figure 19, now all 4 regions, with clearly defined gaps[4] separating them, appear on one hit map. It should be noted here that data presented was taken in absence of any

[4]Gaps between the regions correspond to a non-sensitive area in between regions. For the top HU the size of the gap between regions is 472.5 µm and for the bottom HU it is 486 µm.

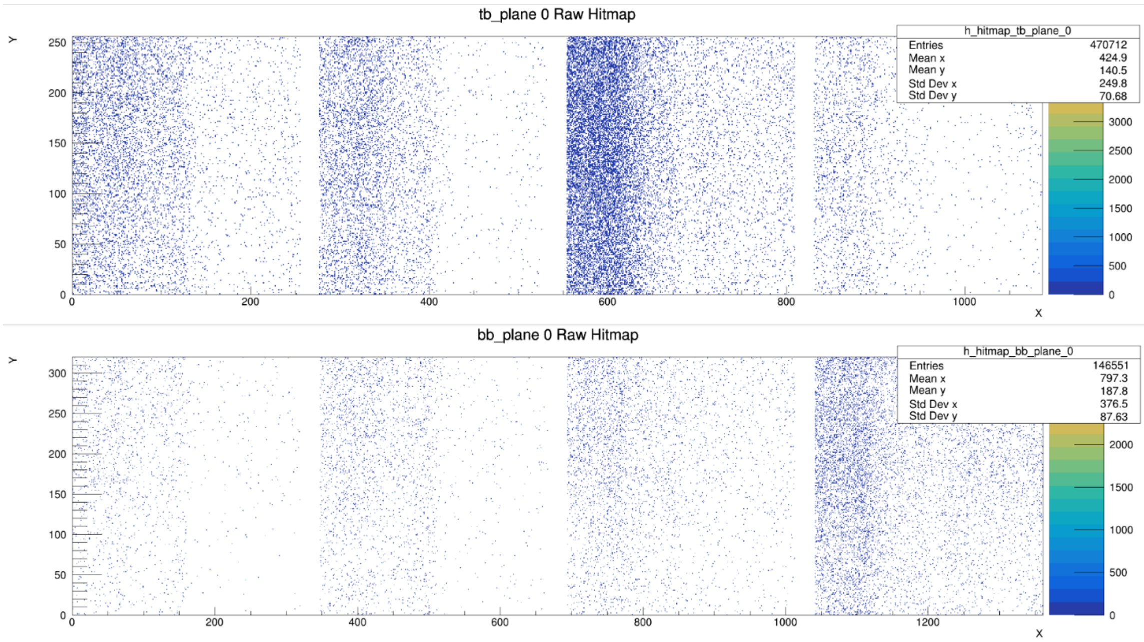

Figure 32: Hit map of the top and bottom HUs for a single babyMOSS sensor, where tb_plane corresponds to the top HU and bb_plane corresponds to the bottom HU. Due to the event converter implementations, a single HU is now represented as a single plane.

particle hits and each of the hit corresponds to the thermal noise inside the sensor. The asymmetry visible in each region is due to the way the bias voltages and currents are distributed to the pixels within each separate region [34].

6.5 Threshold tuning

Fake-hit rate and threshold scans were performed for all 8 regions of each of the telescope planes in order to optimize the threshold values for data acquisition. The goal was to find a value that has minimal fake-hit rate, under 10^{-8} hits/pixel/event, and also that allows detecting muons that deposit less charge. The scans were performed for different V_{casb} (in DAC units) and strobe length (in CC) values. Noisy pixels were identified (the ones that register a hit in more than 0.9% of all events), and FHR scan was re-run again, with the noisy pixels masked. Figure 33 shows FHR scans for babyMOSS-3_4_W05D05, region 2 of the top HU without (left) and with (right) masks. As expected, masking of the noisy pixels significantly decreases the fake-hit rate for the different parameter combinations.

Based on the results of the analysis, a threshold value of 30 DAC (which corresponds to 240 e^-) was chosen to be used for the first run, as it met all of the requirements for the data taking. In addition, the information on noisy pixels, that were identified during the FHR scans, were later-on used to mask them for the data acquisition.

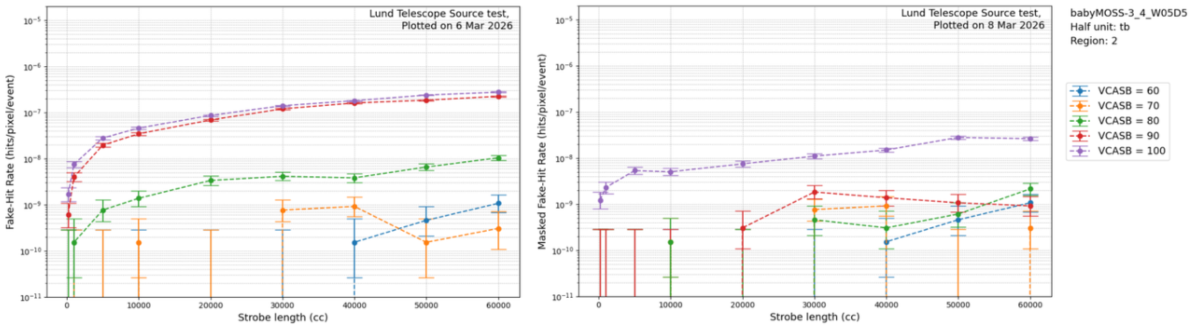

Figure 33: Fake-hit rate values for different V_{casb} settings, as a function of the strobe length for region 2 of top HU of babyMOSS-3_4_W05D05. Plot on the left shows FHR values without masking and plot on the right show FHR values after masking the noisy pixels.

7 Lund Telescope - first results

Once Lund Telescope optimization was complete, a first commission run was performed in order to validate the data acquisition process. Since then, two separate runs with different threshold values, have been performed, each collecting 5000 events.

Firstly, geometry and configuration files were prepared to test analysis using the Corryvreckan framework. However, it should be noted that this software is designed for analysing test beam data, thus there are some limitations as to what can be obtained analysing the cosmic muon data. The main challenge is how the sensor is treated by the software: the fact that the top and bottom HUs of one sensor are treated as two separate planes (this is due to the way Event Converter is currently implemented). Because of this, Corryvreckan will be able to analyse only the events, where a particle has passed the same HU in at least 3 planes, which excludes all inter-HU hits. Since the cosmic muon tracks are non-perpendicular to the telescope, this reduces the already relatively small number of events collected and makes the analysis results not reliable. Nevertheless, further developments are ongoing that would make it possible to integrate both HUs into a standard EUDAQ2 plane, to allow Corryvreckan to perform analysis.

To circumvent this issue, an alternative approach was taken. Dedicated scripts have been implemented, that allow to reconstruct cosmic muon tracks, perform analysis of observed rates, cluster size, residual and angular distributions. The scripts load all raw events and convert them into standard ones, with the help of the implemented converter. First results are presented in the following sections.

7.1 Observed rates

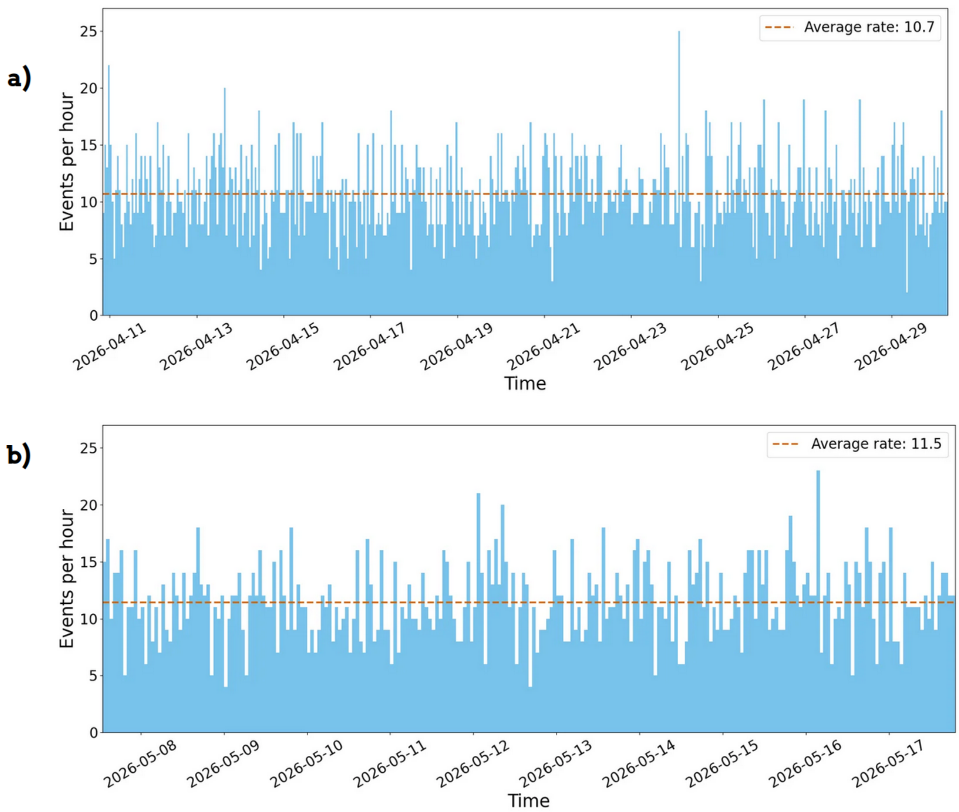

Figure 34: Observed hourly rate of the muons of two separate runs where in a) the threshold was set to 240 e^- and b) to 200 e^-. It should be noted that by the time the data was analysed, the second run with threshold set to 200 e^- has not yet collected 5000 events.

On average, cosmic muon rate at sea level is 1 muon/cm^2/min. For the Lund Telescope, this rate is affected by the geometry of the set-up, event selection and threshold set.

The total hourly observed rate of cosmic muons is plotted in Figure 34 for two different threshold values: a) corresponds to the threshold of 240 e^- and b) to a threshold of 200 e^-. Overall, the number of muons that pass the selection criteria is rather uniform, ranging from 3 to 25 muons per hour. Decreasing the threshold increases the average rate from 10.7 to 11.5 muons per hour. This is because for a lower threshold value, the acceptance rate of the sensors increases, meaning that muons that deposit less charge in the sensor can be detected. This also indicates that there is a higher probability of detecting noise hits, coming from the pixels that are not masked. A possible event is when a noise hit coincides with a muon, that has only passed 2 planes. In general, this muon will not be detected, but if the noise hit appears on a plane that a muon has not passed, this event built by the Data Collector and then written to file.

The sensor geometry impact the rate significantly. The events, in which a particle passes 4 or even all 5 babyMOSS sensors are rare, due to the geometry of the set-up (discussed more in detail in the section 7.4). Analysis done on the first 5000 events collected shows that the average rate of events in which only 3 planes were hit is 7.6 muons per hour, while the events in which either 4 or 5 planes were hit, it goes down to 3.2 muons per hour. Out of 5000, this results in a total of 420 events where all 5 planes.

7.2 Tracks and Cluster Size

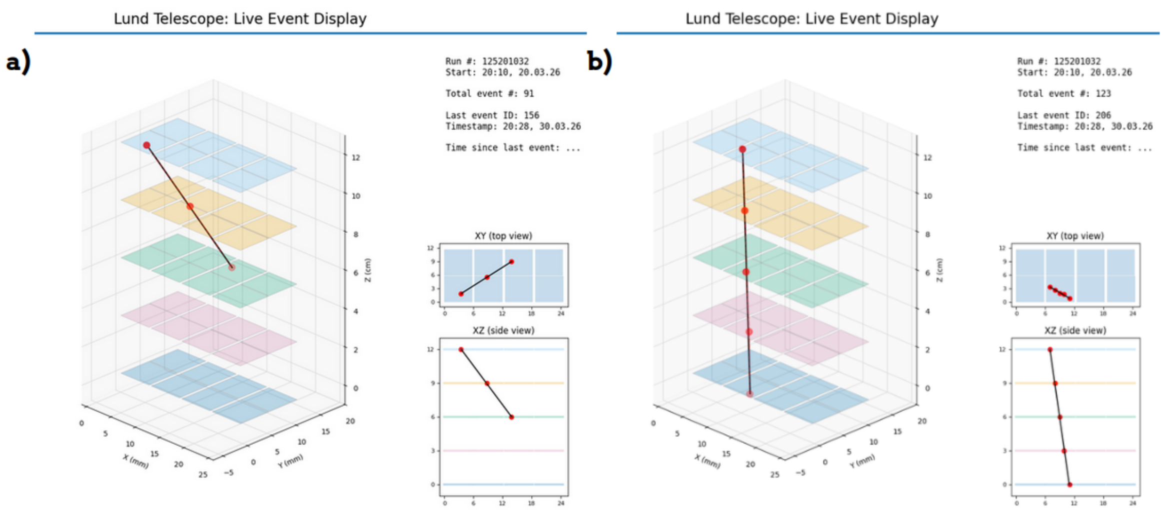

Figure 35: Examples of the events displayed with the Lund Online Monitor where a) corresponds to a track of particle passing 3 sensor planes and b) corresponds to a track where a particle passes all 5 sensor planes. Telescope planes are shown in different colours, displaying the active babyMOSS sensor regions. The online monitor also provides a visualisation of particle tracks in the XY and XZ planes.

Contrary to the test beam, the muons do not hit the telescope perpendicularly. Instead, they traverse the telescope in various incident angles, leaving non-perpendicular tracks in the sensor planes.

Once events are loaded, where at least three planes have a hit, a straight line model is used to fit the hits. Beforehand, hits are combined into clusters in each plane, and their geometric centre is stored as a cluster position. If there is more than one cluster per plane, in the case of noise hit, for example, both get stored to be then used for the fit. Only the track with the best χ^2 is then stored as a muon track.

A dedicated Online Monitor has been created for the Lund Telescope, allowing for a live visualization of the muon hits and the fitted tracks. Figure 35 shows examples of two events, where a particle went across 3 planes (in a)) and 5 planes (in b)). The online monitor also provides a visualization of particle tracks in the XY and XZ planes, allowing to better see particle's track and the number of regions it passes.

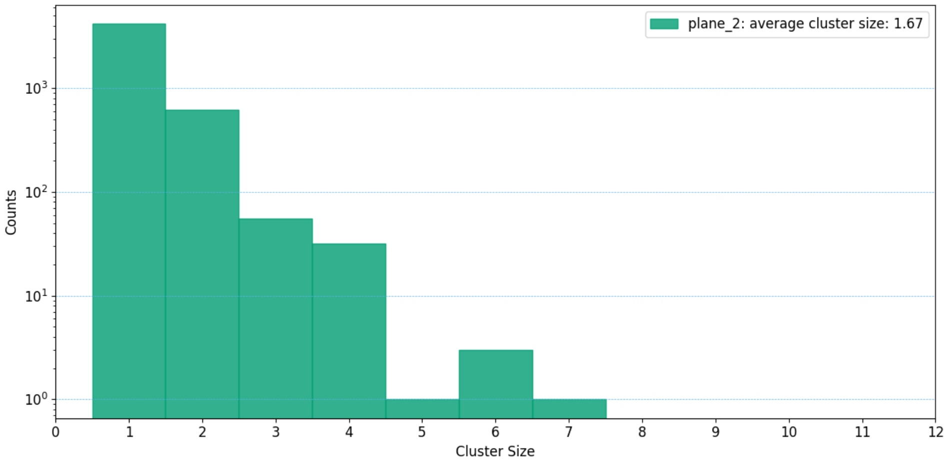

Figure 36: Distribution of the cluster size for the middle plane in the Lund Telescope.

Due to the non-perpendicular muon tracks, the average cluster size is expected to be larger than 1, and surpass the average cluster size, obtained in the test beam. Figure 36 shows cluster size distribution for one of the Lund Telescope planes. For more inclined muon tracks, the cluster size increases, as a larger number of pixels can be sharing the charge deposited by one particle. For more straight tracks, the cluster size is closer to 1, which makes the majority of the hits. It can be also interesting to compare the cluster sizes between the data from the test beam and cosmic muons. Particles coming from a beam and hitting the sensor planes perpendicularly tend to deposit charge in one pixel, sometimes in a few, but the average cluster size for threshold close to 240 e^- is around 1.15, as plotted in Figure 23. For cosmic muons, the average cluster size is close to 1.7, for the geometry of the Lund Telescope. Cluster size distributions for other planes can be found in Appendix C.

7.3 Alignment and residuals

The standard pre-alignment procedure of plotting correlations between the different planes, was not possible to perform for the Lund Telescope, due to the inclined tracks. Instead, alignment was performed manually, using a simple straight line fit model. First, tracking was performed using the data, which was loaded and converted from the raw events. Then, tracking information was analysed and residual distributions were built, calculating residual values for each track in x and y. An example result for plane 0 can be seen in Figure 37 a). The residual distribution in x is not centred at 0, while the residual in y has two separate peaks. All this shows that there is a mismatch between where the particle hit, and where the track was fitted, which could be due to misalignment in the telescope. After extracting the peak position in both x and y coordinates, the information was input as alignment data. Then, planes were realigned according to the input data, tracking performed again and then the residual distributions are built again, calculating residuals in x and y for each track. An example result is visible in Figure 37 b). Overall, this improved the residual values, since both plots show gaussian-shaped peak that is centred at 0. Re-doing this procedure manually over and over again would improve the residual values even further. Overall, the physical alignment between the planes is good, with the misalignment between the planes ranging from 4 µm to 0.1 mm. As such, the alignment input results were used for the rest of the analysis.

A parallel can be made with the alignment that Corryvreckan performs by extracting the peak values of the residuals and re-running the pre-alignment, until the residuals are centred at 0, however it is able to do it over multiple iterations at a relatively high speed [42]. Residual distributions for other planes can be found in Appendix D.

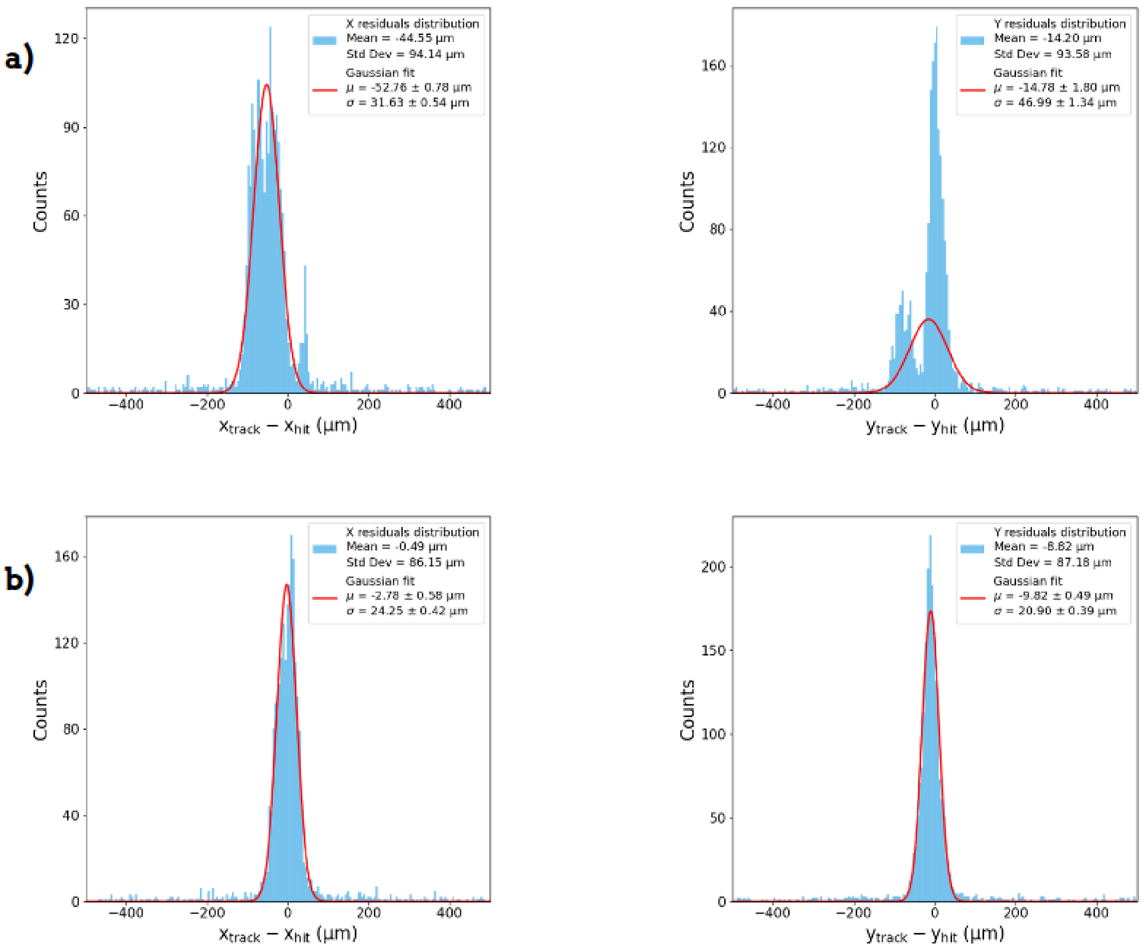

Figure 37: Residual distributions for plane 0 of the Lund Telescope a) before any alignment and b) after repeating alignment procedure, taking into account plane shifts obtained from residual distribution shown in a).

7.4 Angular distribution analysis

Based on available data, at sea level, the cosmic muon flux can be described by:

$$I(\theta) \propto cos^n(\theta)$$

where $n \approx 2$ and θ is the polar angle [48]. This means, that the flux is maximum for $\theta = 0°$ and decreases with increasing angle. However, in this case, this flux is affected by the geometric acceptance of the telescope, and the number of muons measured at a given polar angle will not be equal to the theoretical muon flux at that angle. The geometrical acceptance of the telescope can be defined as

$$\mathrm{N_{meas}}(\theta) \sim \mathrm{I}(\theta) \times \mathrm{A}(\theta)$$

where $\mathrm{N_{meas}}$ corresponds to the measured number of muons at angle θ, I is the actual number and A is the geometric acceptance correction of the Lund Telescope. There are two main contributions to the geometric acceptance correction: the projected detector area, which is proportional to $\cos\theta$ and the solid angle correction, which is proportional to $\sin\theta$. As such, the correction factor used for calculating polar angle distributions was $\mathrm{A}(\theta) \sim \sin\theta\cos\theta$.

Figure 38 shows measured polar angle distributions a) before and b) after applying the correction. The raw distribution is heavily affected by the geometry of the Lund Telescope set-up, because of which,

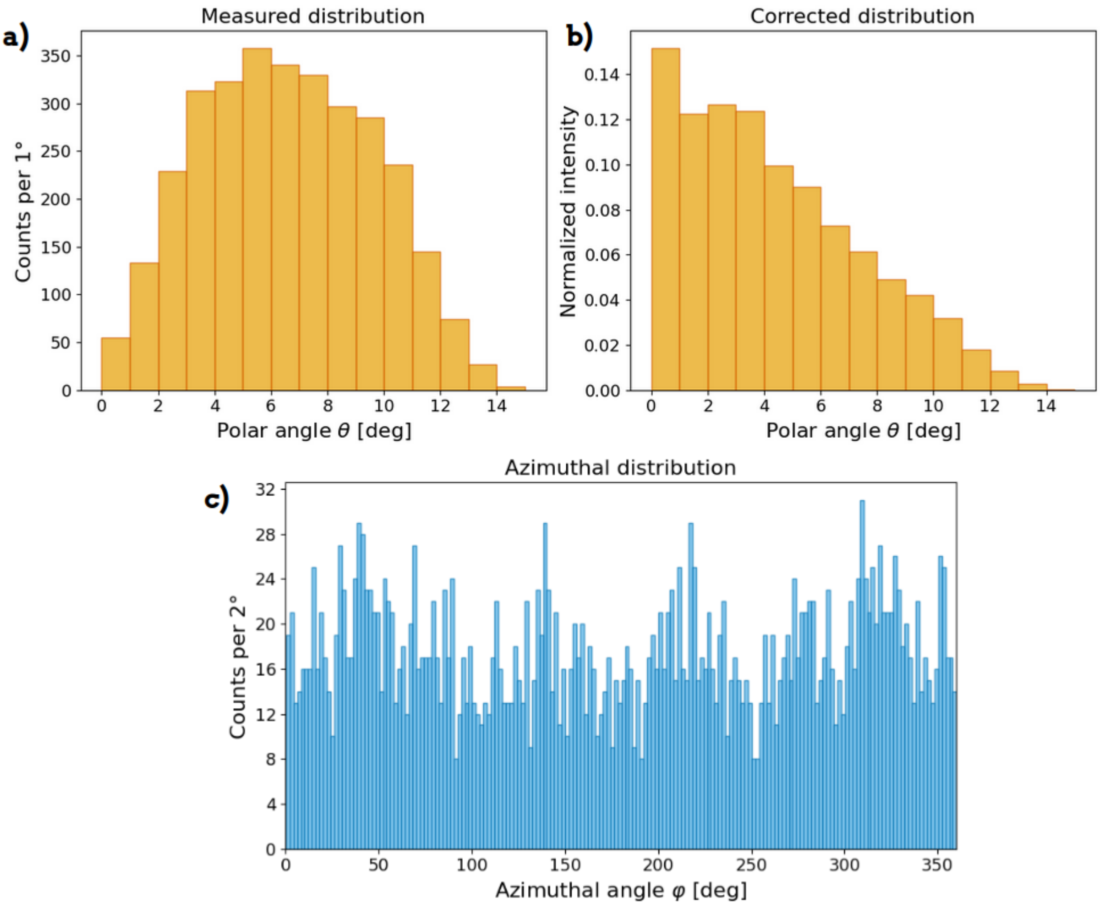

Figure 38: Measured muon angular distribution for a) raw polar angle distribution, b) corrected polar angle distribution, showing normalized intensity and c) azimuthal angle distribution.

the histograms do not peak at $\sim 0°$. Once geometrical corrections applied, the measured most probable polar angle value is around $\sim 0°$, which is as expected. It should be noted that for the polar angle distribution, the position of the peak is also affected by the event selection. Most events recorded go through only 3 planes, which means that the measured polar angle for these tracks is larger than 0°. If the event selection was restricted even further, and only the events in which a particle traversed 4 or even all 5 planes were recorded, the peak of the measured polar distribution would shift closer to 0°.

As for the azimuthal angle, shown in Figure 38 c), the distribution is fairly uniform, which is expected, however, collecting more events would make this distribution even more uniform.

7.5 Further studies

The analysis results, presented in this chapter correspond to just the start of what should and could be achieved. The final goal of the Lund Telescope is to be able to use it as an alternative to test beams. As such, analysis of the detection efficiency and spatial resolution need to be performed.

To be able to do that, first and foremost, a sufficient amount of statistics must be collected. With cosmic muons, as can be concluded from the observed event rate, this can take up to a few months. In addition, it is crucial to improve the event converter of EUDAQ2 in order to have a babyMOSS sensor represented as a single plane. This would allow performing analysis using the Corryvreckan framework, without losing the inter-HU events.

Once these things established, the Lund Telescope can be successfully used to characterize other sensor prototypes.

8 Conclusion

This thesis presented two distinct methods of characterising pixel sensors using high-energy particles. The sensors used are prototypes, developed for the upcoming ITS3 upgrade in ALICE. First, the test beam of September 2025 was presented, taking place at the PS at CERN, where a 7 GeV/c negative pion beam was used. The telescope was built containing 6 babyMOSS tracking planes 1 DUT. 2 separate babyMOSS DUTs of differing geometries were tested in the telescope, with only the region 0 of top and bottom half-units enabled. The telescope triggering scheme, which follows a standard test beam triggered read out, is reviewed. The set-up used 2 scintillators, placed before the first and after the last tracking plane, working in coincidence. Trigger cycle in the sensors was initiated, once a particle passed both scintillators. Fake-hit rate and threshold scans were performed in order to optimize the threshold of each sensor.

The measurements performed during the test beam were of detection efficiency and spatial resolution. For detection efficiency, it was shown that a larger pixel pitch gives a higher detection efficiency, however increasing the size of the gap between the pixels worsens the detection efficiency. This is due to the amount of charge sharing, which directly influences the detection efficiency. These result are consistent with previous studies. Analysis of the spatial resolution show that both pixel pitches, achieve a better spatial resolution, that their respective binary resolution, due to the fact that, on average, the cluster size is larger than 1. However, it is shown that the target spatial resolution of 5 µm for ITS3 is achieved only by the pixel geometry of the bottom half-unit.

In the second part of this project, an alternative to test beams was presented: the use of cosmic muons as a way to characterize sensor prototypes. Because the LHC will start its Long Shutdown 3 this year and there is going to be no beam available at CERN for the upcoming few years, a proposed solution is to use cosmic rays as a source of high-energy particles. For this purpose a compact telescope was built in Lund. The triggering scheme was optimized to function without having any scintillators in the set-up, in a so-called continuous data acquisition mode. By refining the triggering parameters it was possible to have the telescope operating at a 99% active duty time. Important software developments had to be implemented to take into consideration the data acquisition process, as well as event selection, to deal with the large amount of empty data and/or noise being sent out during each trigger cycle.

First commission runs helped to validate the data acquisition process and long term data taking runs were started, with the first one collecting 5000 muon events in almost 20 days. Analysis using the Corryvreckan framework, as was done for the data collected in the test beam, was not possible at the time, due to the limited amount of statistics collected. As such, first analysis was performed using in-house scripts, that provided different insights into the data collected. Alignment was performed manually by first fitting the hit tracks and then calculating the residuals, extracting the shift position, inputting it as alignment data, which is then used to re-fit tracks and to re-calculate the residuals again. This improved the overall alignment of the telescope, however more automated methods need to be used in order to obtain more reliable results. The observed rate is around 10 muons per hour, indicating that the geometry of the set-up limits the events that are accepted. Cluster size studies show that for non-perpendicular tracks, the average cluster size increases up to about 1.7. Overall, the data acquisition process was validated and the software implementations represent an important work done towards having a functional and compact telescope at Lund University.

That being said, once enough statistics collected, alignment procedure and analysis must be performed. Event converter of EUDAQ2 should be modified, to represent a single sensor as one plane and Corryvreckan could be used to analyse the data. Of particular interest is the sensor detection efficiency studies with the cosmic muons. Further analysis can also be done to estimate the spatial resolution, although the non-perpendicular tracks and large cluster sizes may bias the results. Moreover, a possibility of using new sensor prototypes should be considered, allowing for sensor characterization, without having a beam.

References

[1] B. R. Martin and G. Shaw. *Particle Physics*. Wiley, 2017.

[2] C. Grupen and B. Shwartz. *Particle Detectors*. Cambridge University Press, 2008.

[3] F. Hartmann. *Evolution of Silicon Sensor Technology in Particle Physics*. Springer, 2017.

[4] *Facts and figures about the LHC*. https://home.cern/resources/faqs/facts-and-figures-about-lhc. Accessed: 2026-04-30.

[5] The ALICE collaboration. *Technical Design report for the ALICE Inner Tracking System 3 - ITS3 ; A bent wafer-scale monolithic pixel detector*. Tech. rep. Geneva: CERN, 2024. URL: https://cds.cern.ch/record/2890181.

[6] S. Navas et al. "Review of particle physics". In: *Phys. Rev. D* 110.3 (2024), p. 030001. DOI: 10.1103/PhysRevD.110.030001.

[7] L. Rossi et al. *Pixel Detectors: From Fundamentals to Applications*. Springer, 2006.

[8] H. Kolanoski and N. Wermes. *Particle Detectors: fundamentals and applications*. Oxford University Press, 2020.

[9] S. Seidel. "Silicon strip and pixel detectors for particle physics experiments". In: *Phys. Rep.* 828 (2019). DOI: https://doi.org/10.1016/j.physrep.2019.09.003.

[10] W. R. Leo. *Techniques for Nuclear and Particle Physics Experiments: A How-to Approach*. Springer-Verlag, 1994.

[11] H. G. Moser. "Silicon detector systems in high energy physics". In: *Prog. Part. Nucl. Phys.* 63 (2009). DOI: 10.1016/j.ppnp.2008.12.002.

[12] S. Senyukov et al. "Charged particle detection performances of CMOS pixel sensors produced in a 0.18 μm process with a high resistivity epitaxial layer". In: *Nucl. Instrum. Meth. A* (2013). DOI: https://doi.org/10.1016/j.nima.2013.03.017. URL: https://www.sciencedirect.com/science/article/pii/S0168900213002945.

[13] M. Winter and M. Deveaux. "Complementary Metal-Oxide-Semiconductor (CMOS) Pixel Sensors". In: *Handbook of Particle Detection and Imaging*. Ed. by I. Fleck et al. Springer International Publishing, 2021. DOI: 10.1007/978-3-319-93785-4_55.

[14] R. Turchetta et al. "A monolithic active pixel sensor for charged particle tracking and imaging using standard VLSI CMOS technology". In: *Nucl. Instrum. Meth. A* 458.3 (2001), pp. 677–689. DOI: https://doi.org/10.1016/S0168-9002(00)00893-7.

[15] *Analyzing the LHC Magnet Quenches*. https://spectrum.ieee.org/analyzing-the-lhc-magnet-quenches.

[16] *ALICE journey*. https://alice.cern/timeline. Accessed: 2026-04-23.

[17] *ALICE Collaboration*. https://alice-collaboration.web.cern.ch/. Accessed: 2026-04-22.

[18] R. Pasechnik and M. Šumbera. *Phenomenological Review on Quark–Gluon Plasma: Concepts vs. Observations*. Jan. 2017. DOI: 10.3390/universe3010007. URL: http://dx.doi.org/10.3390/universe3010007.

[19] The ALICE Collaboration. "The ALICE experiment: a journey through QCD". In: *Eur. Phys. J. C* (2024).

[20] The ALICE Collaboration. "The ALICE experiment at the CERN LHC". In: *JINST* 3 (2008), S08002.

[21] W. H. Trzaska. “New ALICE detectors for Run 3 and 4 at the CERN LHC”. In: *Nucl. Instrum. Meth. A* 958 (2020). Proceedings of the Vienna Conference on Instrumentation 2019, p. 162116. DOI: 10.1016/j.nima.2019.04.070.

[22] *The ALICE Time Projection Chamber*. https://alice-tpc.web.cern.ch/content/alice-time-projection-chamber.

[23] *ALICE TRD*. https://alice-collaboration.web.cern.ch/menu_proj_items/trd. Accessed: 2026-04-23.

[24] *ALICE TOF*. https://alice-collaboration.web.cern.ch/menu_proj_items/tof. Accessed: 2026-04-23.

[25] *ALICE HMPID*. https://alice-collaboration.web.cern.ch/menu_proj_items/HMPID. Accessed: 2026-04-23.

[26] *ALICE PHOS*. https://alice-collaboration.web.cern.ch/menu_proj_items/phos-cpv. Accessed: 2026-04-23.

[27] *ALICE EMCAL*. https://alice-collaboration.web.cern.ch/menu_proj_items/emcal. Accessed: 2026-04-23.

[28] S. Acharya et al. “ALICE upgrades during the LHC Long Shutdown 2”. In: *JINST* 19.05 (May 2024). DOI: 10.1088/1748-0221/19/05/P05062.

[29] *ALICE ITS*. https://alice-collaboration.web.cern.ch/ALICE_ITS. Accessed: 2026-04-23.

[30] L. Musa. *Letter of Intent for an ALICE ITS Upgrade in LS3*. Tech. rep. CERN, 2019.

[31] M. Šuljić. “ALPIDE: the Monolithic Active Pixel Sensor for the ALICE ITS upgrade”. In: *Journal of Instrumentation* 11.11 (Nov. 2016), p. C11025. DOI: 10.1088/1748-0221/11/11/C11025. URL: https://doi.org/10.1088/1748-0221/11/11/C11025.

[32] A. Isakov et al. “ALICE ITS2: overview and performance”. In: *JINST* 20.07 (July 2025). DOI: 10.1088/1748-0221/20/07/C07026.

[33] V. Sarritzu. “ITS3: the ALICE Inner Tracking System upgrade”. In: *PoS* TIPP2023 (2025), p. 126. DOI: 10.22323/1.468.0126.

[34] O. Abdelrahman et al. “Characterisation of the first wafer-scale prototype for the ALICE ITS3 upgrade: The monolithic stitched sensor (MOSS)”. In: *Nucl. Instrum. Meth. A* 1086 (2026), p. 171297. ISSN: 0168-9002. DOI: https://doi.org/10.1016/j.nima.2026.171297. URL: https://www.sciencedirect.com/science/article/pii/S0168900226000239.

[35] P. Vicente Leitao et al. “Development of a Stitched Monolithic Pixel Sensor prototype (MOSS chip) towards the ITS3 upgrade of the ALICE Inner Tracking System”. In: *JINST* 18.01 (Jan. 2023), p. C01044. DOI: 10.1088/1748-0221/18/01/C01044.

[36] *ALICE ITS3*. https://alice-collaboration.web.cern.ch/menu_proj_items/ITS-3.

[37] W. Snoeys et al. “Optimization of a 65 nm CMOS imaging process for monolithic CMOS sensors for high energy physics”. In: *PoS* Pixel2022 (2023). DOI: 10.22323/1.420.0083.

[38] F. King et al. *Review of prototypes developed in a 65 nm CMOS imaging technology in view of vertexing applications at a future lepton collider*. 2026. arXiv: 2602.14900 [physics.ins-det]. URL: https://arxiv.org/abs/2602.14900.

[39] E. Montbarbon et al. “The New CERN East Area Primary and Secondary Beams”. In: *Proc. 10th International Particle Accelerator Conference (IPAC’19)*. Geneva, Switzerland: JACoW Publishing, 2019, pp. 3730–3733. DOI: doi:10.18429/JACoW-IPAC2019-THPGW062.

[40] *Experimental Areas: T10*. https://be-dep-ea.web.cern.ch/experimental-areas/east-area/t10. Accessed: 2026-04-20.

[41] P. Ahlburg et al. "EUDAQ—a data acquisition software framework for common beam telescopes". In: *Journal of Instrumentation* 15.01 (2020), P01038. DOI: 10.1088/1748-0221/15/01/P01038. URL: https://doi.org/10.1088/1748-0221/15/01/P01038.

[42] D. Dannheim et al. "Corryvreckan: a modular 4D track reconstruction and analysis software for test beam data". In: *Journal of Instrumentation* 16.03 (2021), P03008. DOI: 10.1088/1748-0221/16/03/P03008. URL: https://doi.org/10.1088/1748-0221/16/03/P03008.

[43] J. Kröger, S. Spannagel, and M. Williams. "User Manual for the Corryvreckan Test Beam Data Reconstruction Framework, Version 2.0". In: (Apr. 2026).

[44] P. K. F. Grieder. *Cosmic Rays at Earth: Researcher's Reference Manual and Data Book*. Elsevier, 2001.

[45] A. Bettini. *Introduction to Elementary Particle Physics*. Cambridge University Press, 2008.

[46] Y. Liu et al. "EUDAQ2—A flexible data acquisition software framework for common test beams". In: *JINST* 14 (2019), P10033. DOI: 10.1088/1748-0221/14/10/P10033.

[47] Y. Liu. "EUDAQ2 User Manual". In: (2017). URL: https://eudaq.github.io.

[48] S. Cecchini and M. Spurio. "Atmospheric muons: experimental aspects". In: *Geoscientific Instrumentation, Methods and Data Systems* 1.2 (2012), pp. 185–196. DOI: 10.5194/gi-1-185-2012. URL: https://gi.copernicus.org/articles/1/185/2012/.

A Residuals and χ^2/ndf

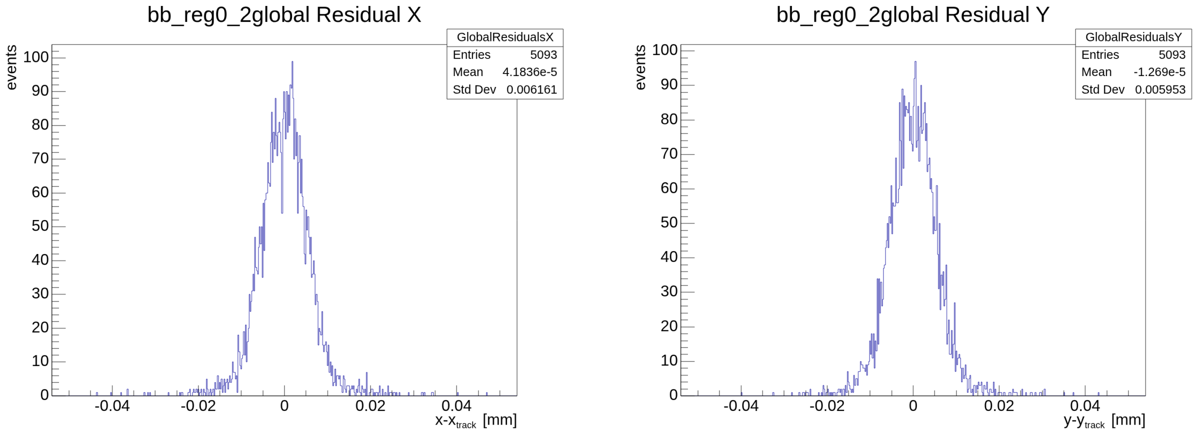

(a) Residual in global X

(b) Residual in global Y

Figure 39: Residuals of region 0 of the bottom half-unit of tracking plane 2 (reference plane).

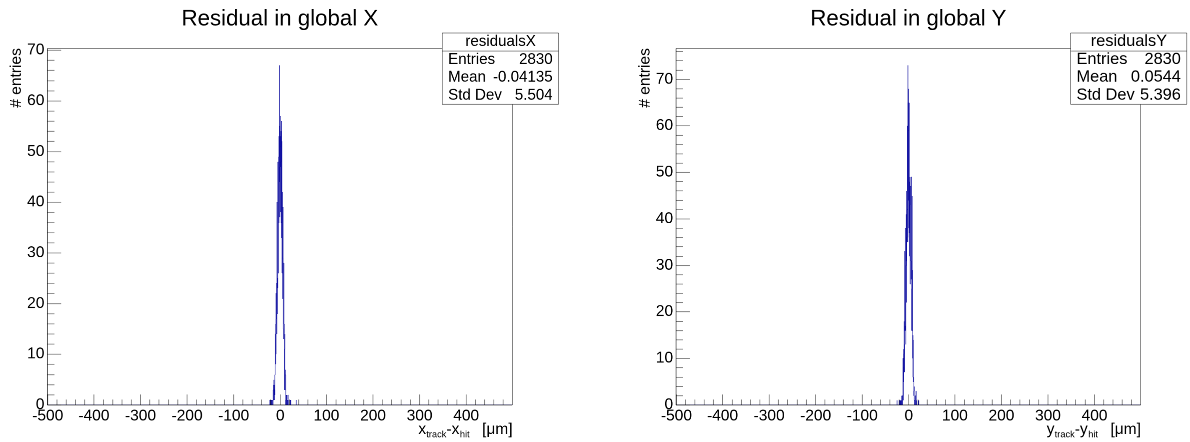

(a) Residual in global X

(b) Residual in global Y

Figure 40: Residuals of region 0 of the bottom half-unit of the DUT (babyMOSS-2_5_W06D0).

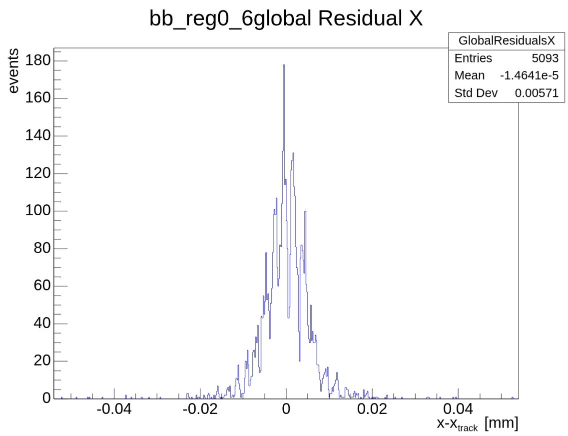

(a) Residual in global X

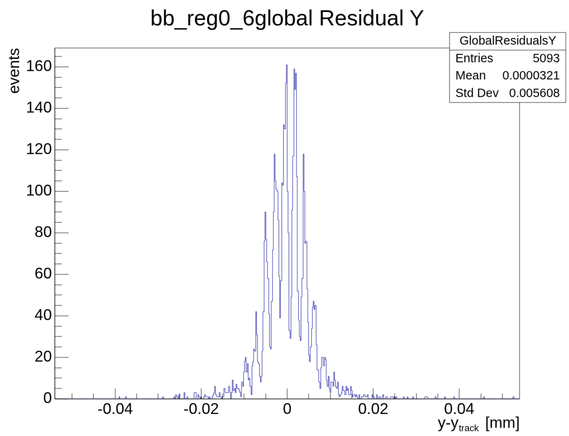

(b) Residual in global Y

Figure 41: Residuals of region 0 of the bottom half-unit of tracking plane 6.

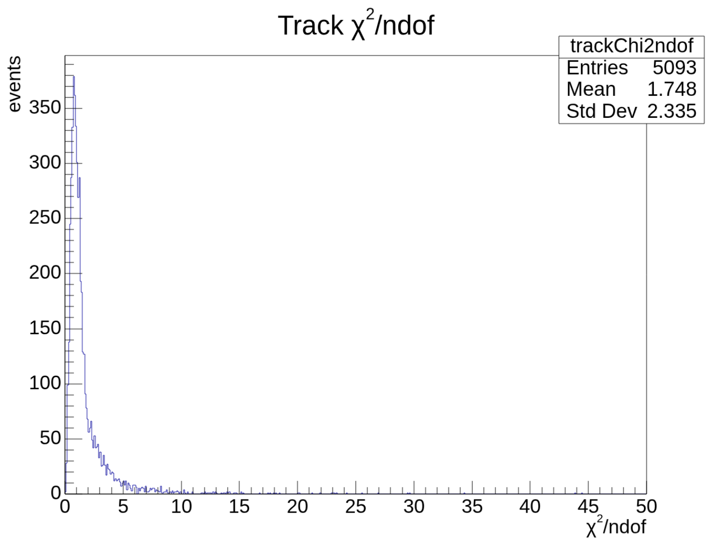

Figure 42: χ^2/ndof for region 0 of the bottom half-unit of babyMOSS-2_5_W06D0 (DUT).

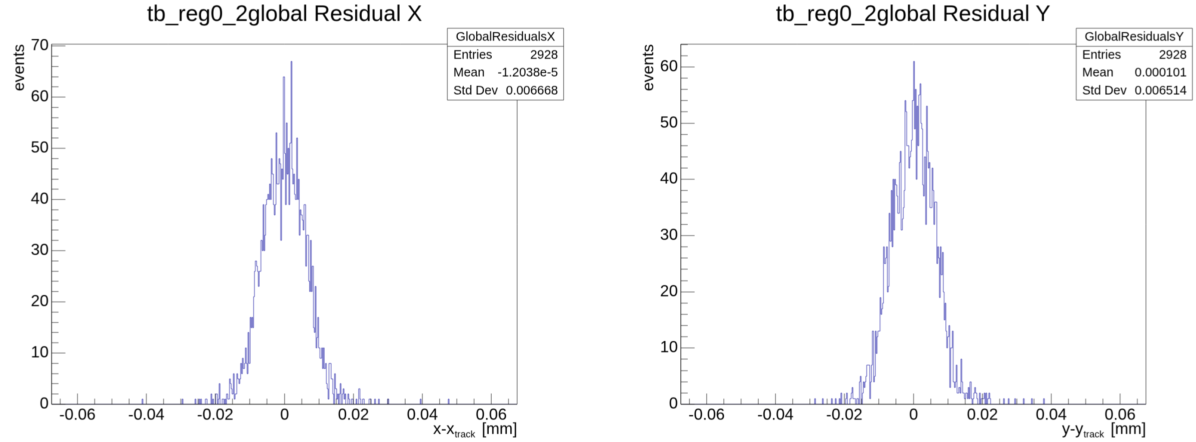

(a) Residual in global X

(b) Residual in global Y

Figure 43: Residuals of region 0 of the top half-unit of tracking plane 2 (tracking plane).

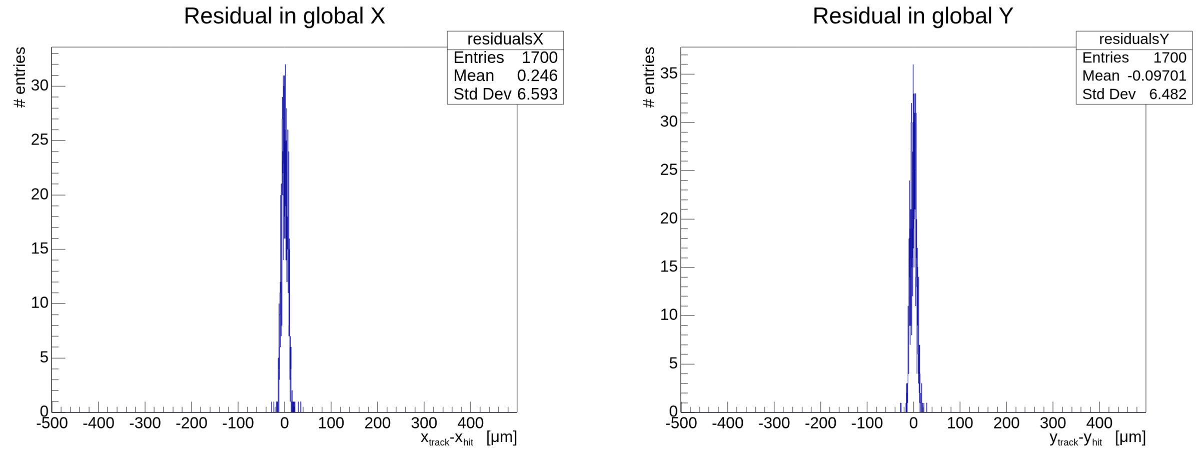

(a) Residual in global X

(b) Residual in global Y

Figure 44: Residuals of region 0 of the top half-unit of the DUT (babyMOSS-2_5_W06D0).

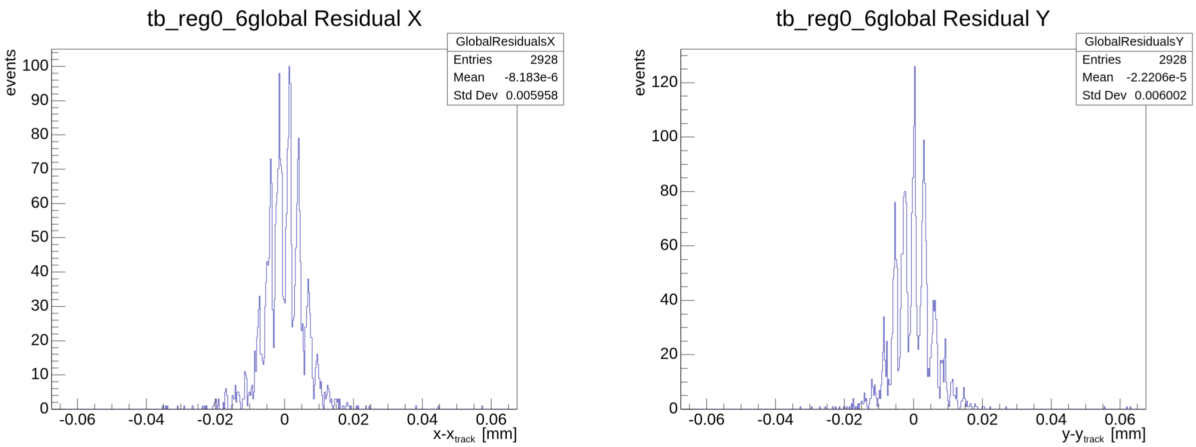

(a) Residual in global X

(b) Residual in global Y

Figure 45: Residuals of region 0 of the top half-unit of tracking plane 6.

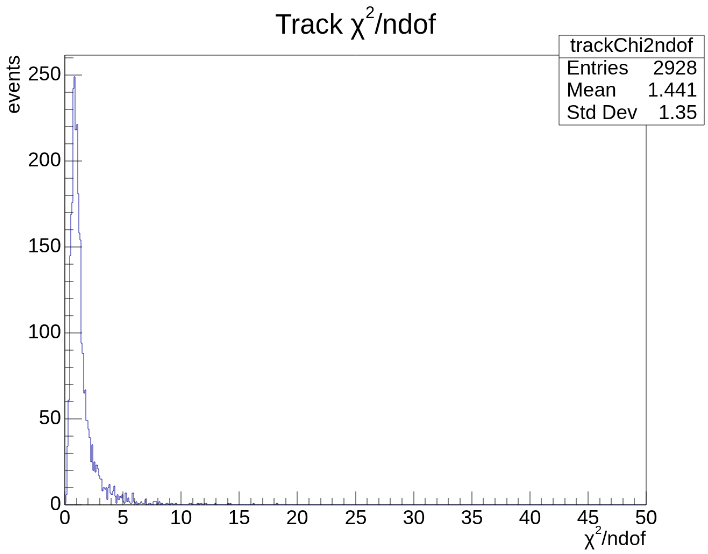

Figure 46: χ^2/ndof for region 0 of the top half-unit of babyMOSS-2_5_W06D0 (DUT).

B Correlation plots

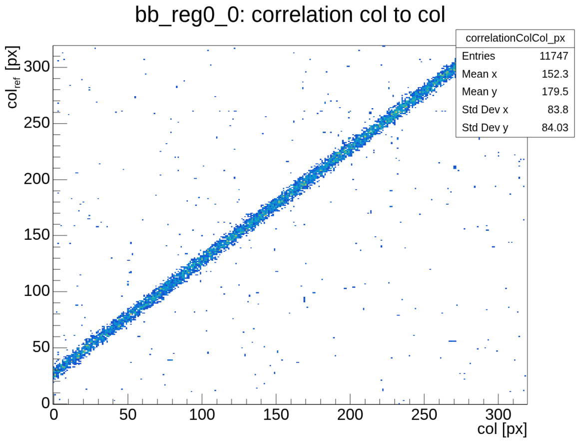

(a) Column to column correlation

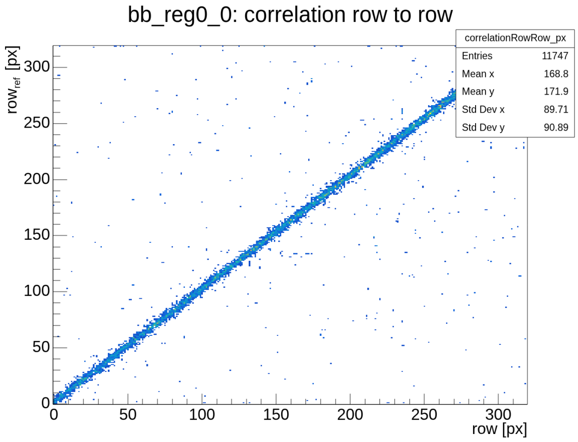

(b) Row to row correlation

Figure 47: Column to column (x-x) and row to row (y-y) correlations for bottom half-unit of tracking plane 0, with regards to tracking plane 2 (reference plane).

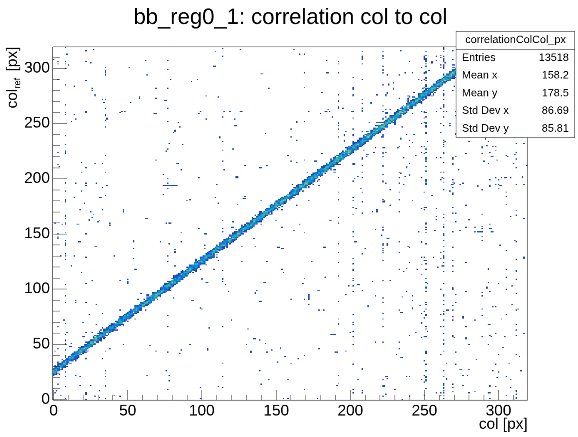

(a) Column to column correlation

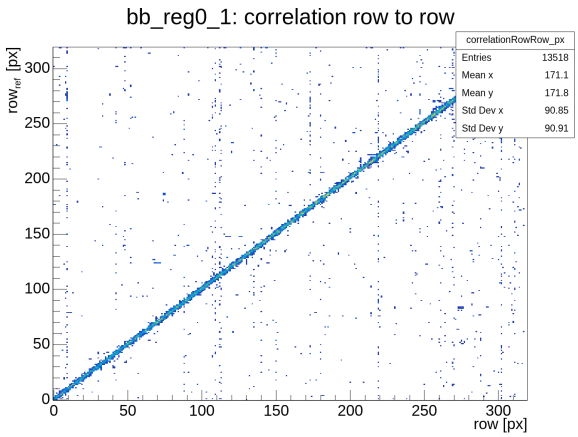

(b) Row to row correlation

Figure 48: Column to column (x-x) and row to row (y-y) correlations for bottom half-unit of tracking plane 1, with regards to tracking plane 2 (reference plane).

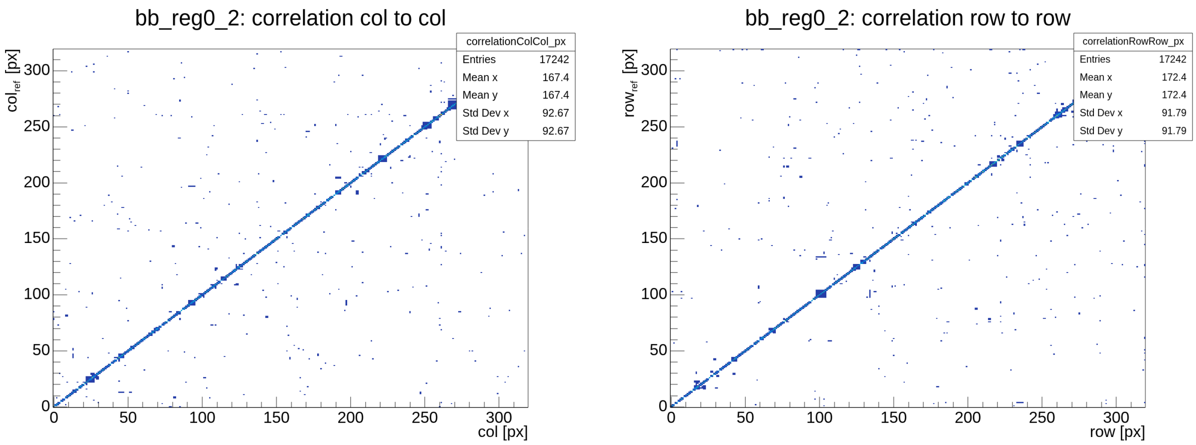

(a) Column to column correlation

(b) Row to row correlation

Figure 49: Column to column (x-x) and row to row (y-y) correlations for bottom half-unit of tracking plane 2, with regards to itself (reference plane).

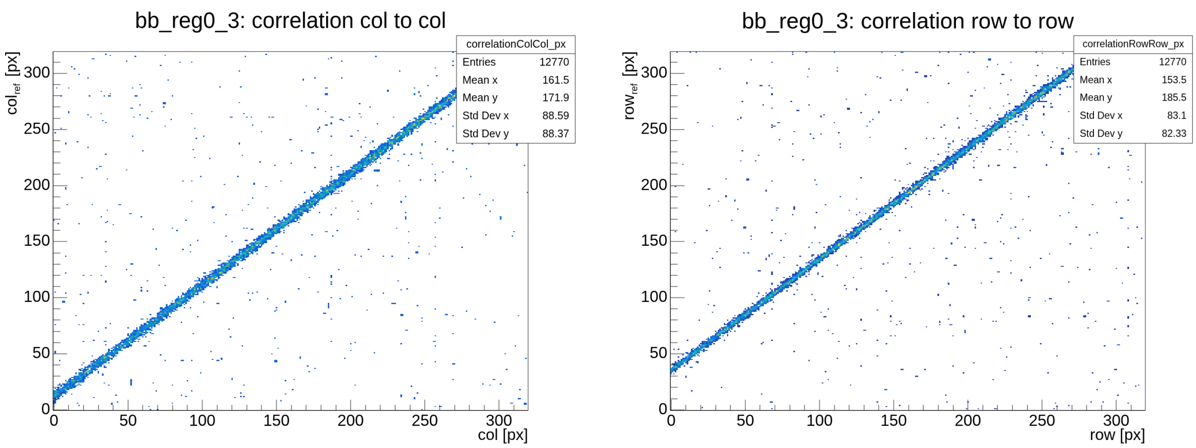

(a) Column to column correlation

(b) Row to row correlation

Figure 50: Column to column (x-x) and row to row (y-y) correlations for bottom half-unit of DUT (babyMOSS-2_5_W06D0), with regards to tracking plane 2 (reference plane).

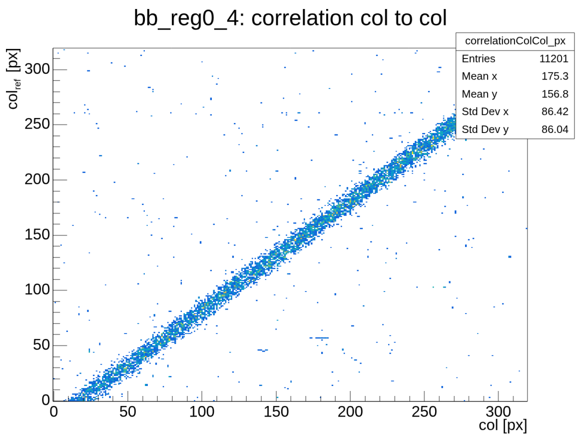

(a) Column to column correlation

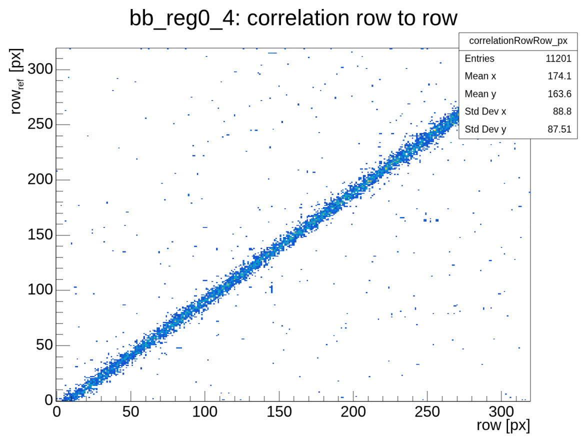

(b) Row to row correlation

Figure 51: Column to column (x-x) and row to row (y-y) correlations for bottom half-unit of tracking plane 4, with regards to tracking plane 2 (reference plane).

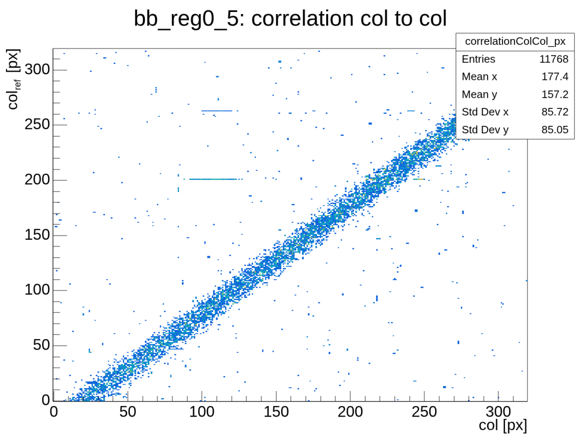

(a) Column to column correlation

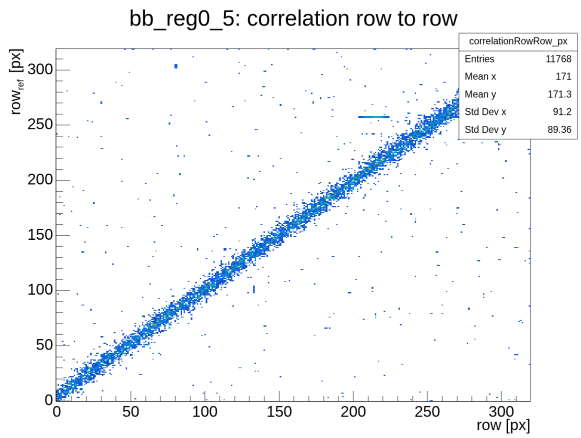

(b) Row to row correlation

Figure 52: Column to column (x-x) and row to row (y-y) correlations for bottom half-unit of tracking plane 5, with regards to tracking plane 2 (reference plane).

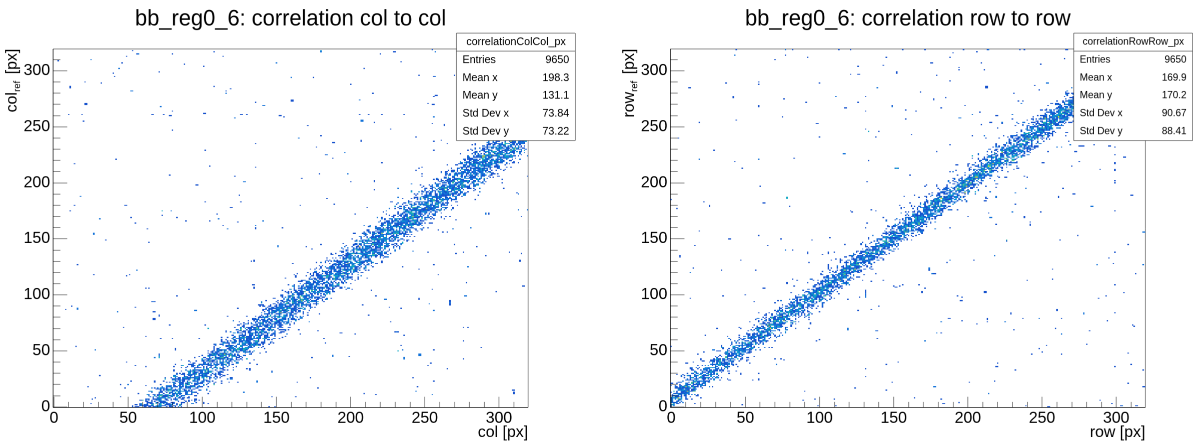

(a) Column to column correlation

(b) Row to row correlation

Figure 53: Column to column (x-x) and row to row (y-y) correlations for bottom half-unit of tracking plane 6, with regards to tracking plane 2 (reference plane).

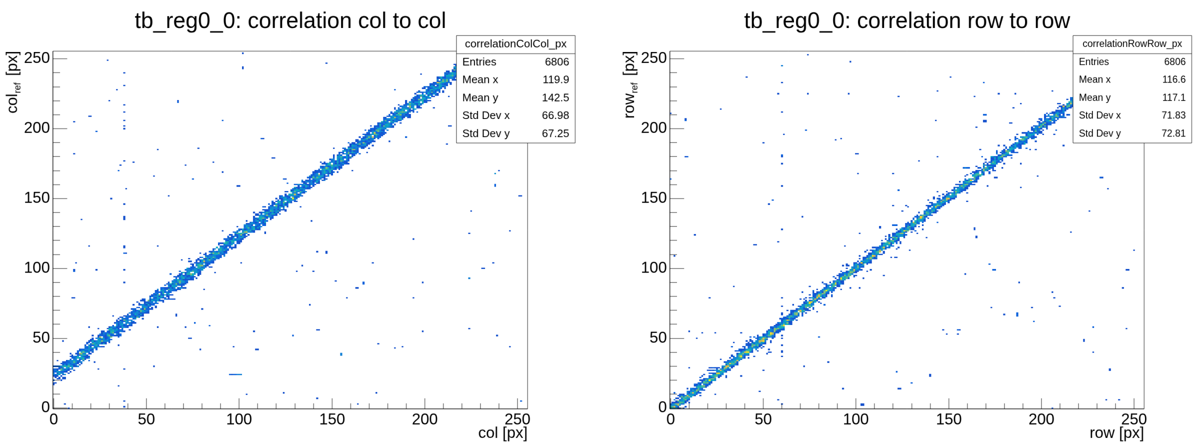

(a) Column to column correlation

(b) Row to row correlation

Figure 54: Column to column (x-x) and row to row (y-y) correlations for top half-unit of tracking plane 0, with regards to tracking plane 2 (reference plane).

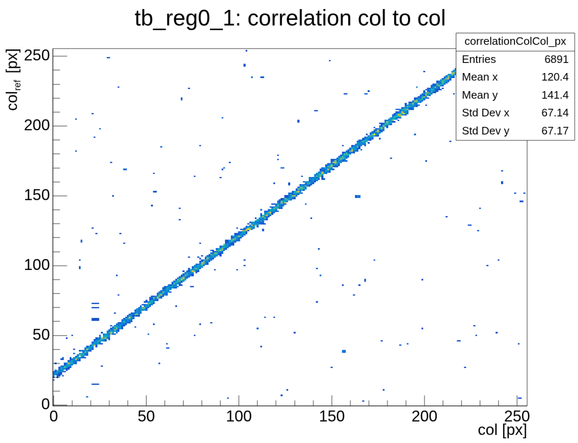

(a) Column to column correlation

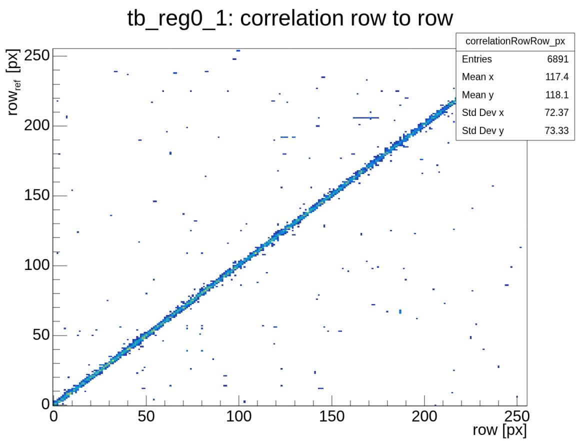

(b) Row to row correlation

Figure 55: Column to column (x-x) and row to row (y-y) correlations for top half-unit of tracking plane 1, with regards to tracking plane 2 (reference plane).

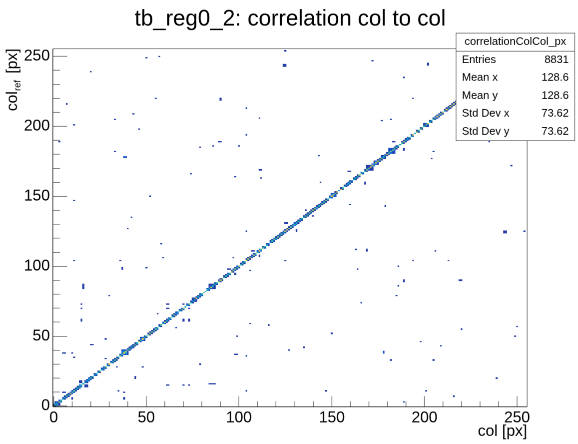

(a) Column to column correlation

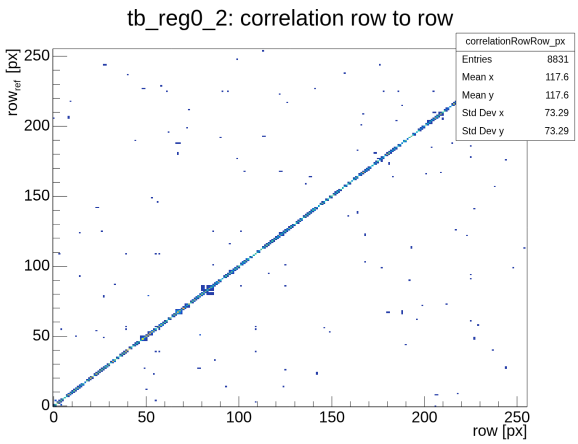

(b) Row to row correlation

Figure 56: Column to column (x-x) and row to row (y-y) correlations for top half-unit of tracking plane 2, with regards to itself (reference plane).

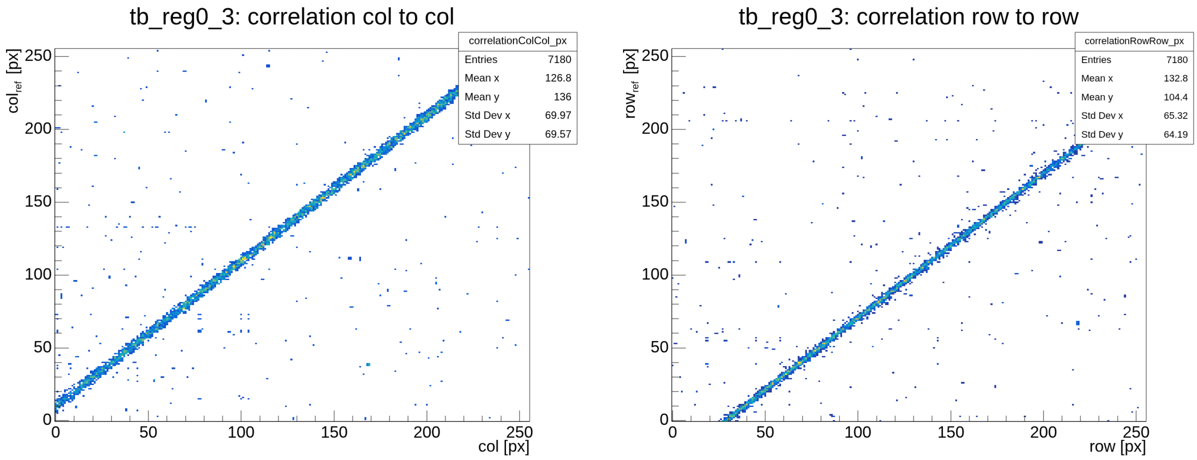

(a) Column to column correlation

(b) Row to row correlation

Figure 57: Column to column (x-x) and row to row (y-y) correlations for top half-unit of DUT (babyMOSS-2_5_W06D0), with regards to tracking plane 2 (reference plane).

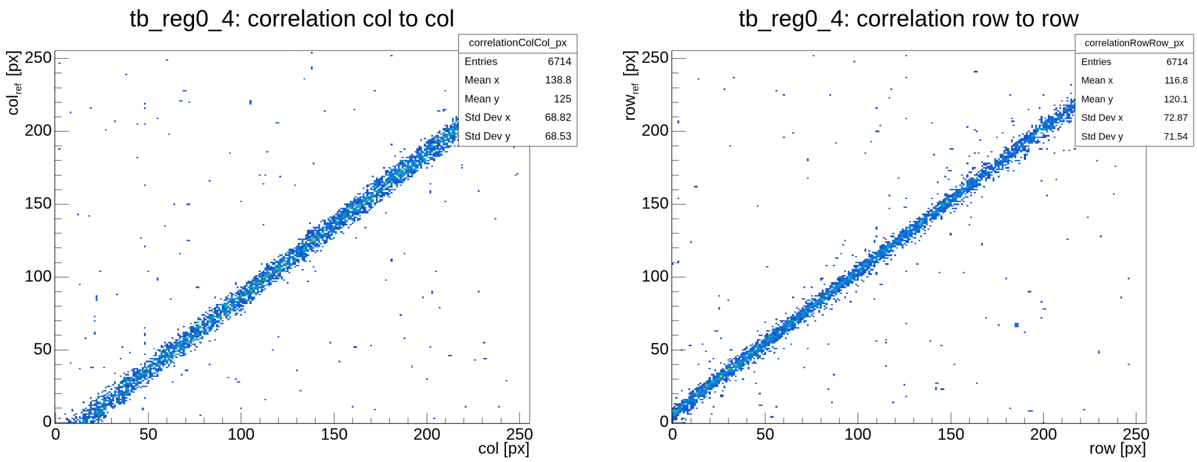

(a) Column to column correlation

(b) Row to row correlation

Figure 58: Column to column (x-x) and row to row (y-y) correlations for top half-unit of tracking plane 4, with regards to tracking plane 2 (reference plane).

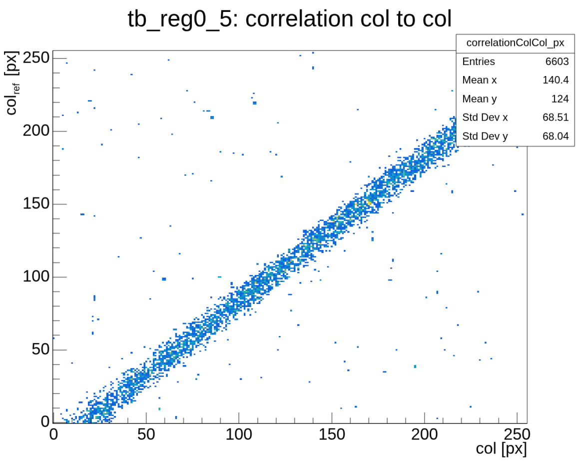

(a) Column to column correlation

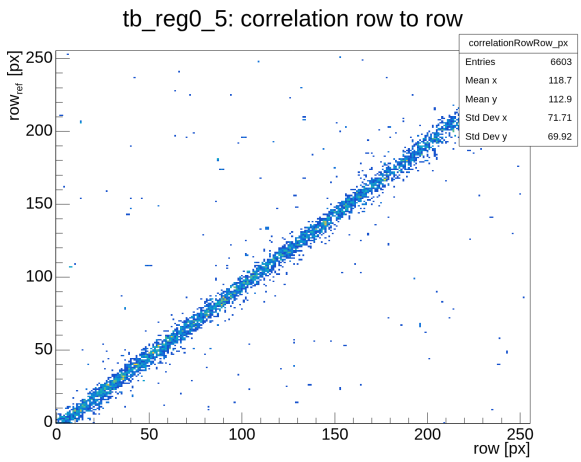

(b) Row to row correlation

Figure 59: Column to column (x-x) and row to row (y-y) correlations for top half-unit of tracking plane 5, with regards to tracking plane 2 (reference plane).

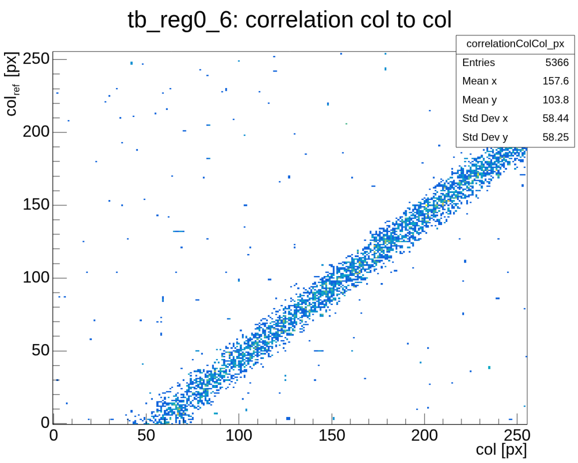

(a) Column to column correlation

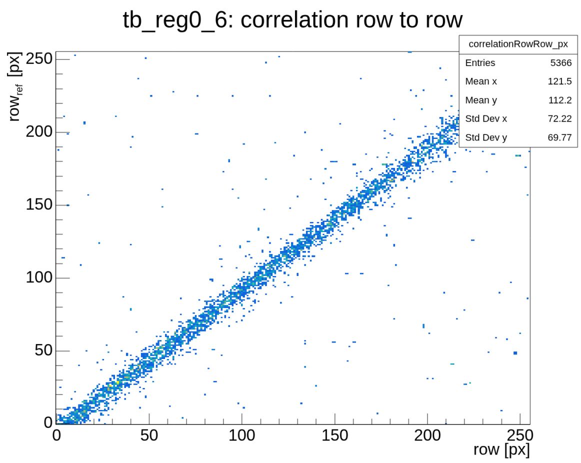

(b) Row to row correlation

Figure 60: Column to column (x-x) and row to row (y-y) correlations for top half-unit of tracking plane 6, with regards to tracking plane 2 (reference plane).

C Cluster sizes for Lund Telescope planes

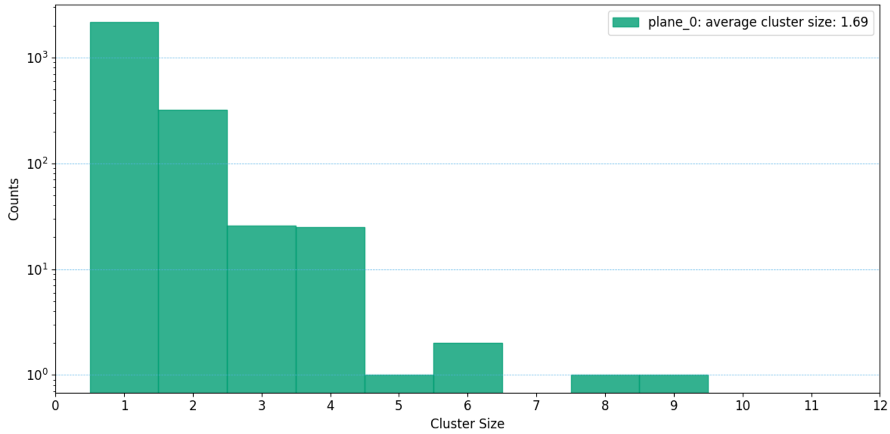

Figure 61: Cluster size distribution for plane 0.

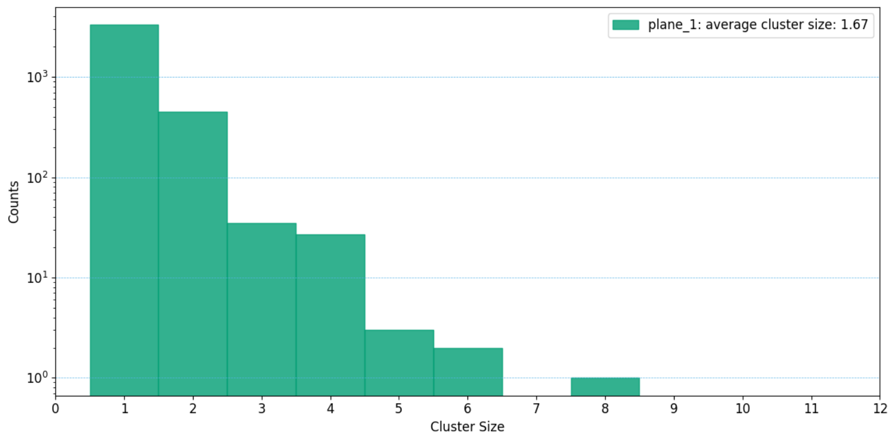

Figure 62: Cluster size distribution for plane 1.

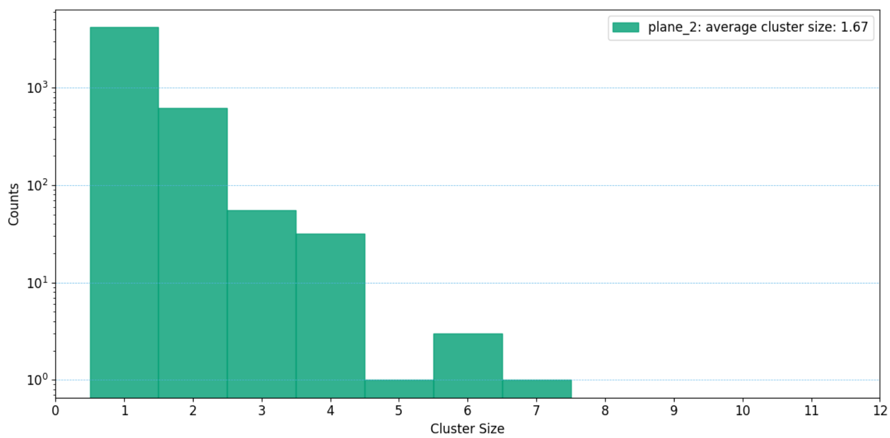

Figure 63: Cluster size distribution for plane 2.

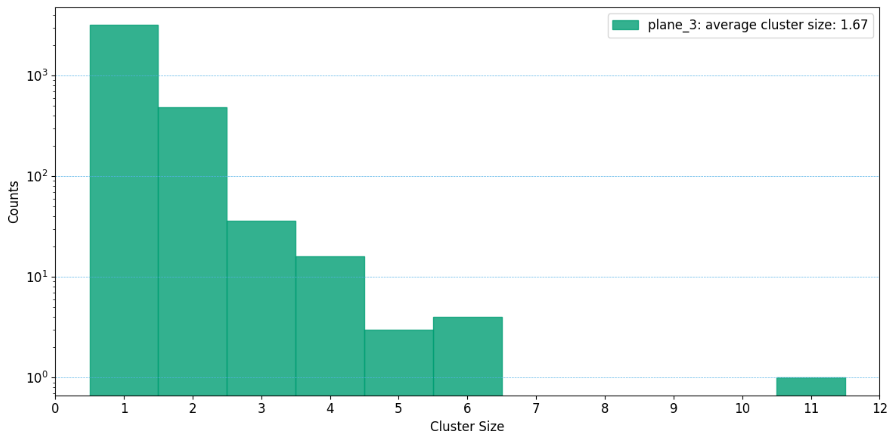

Figure 64: Cluster size distribution for plane 3.

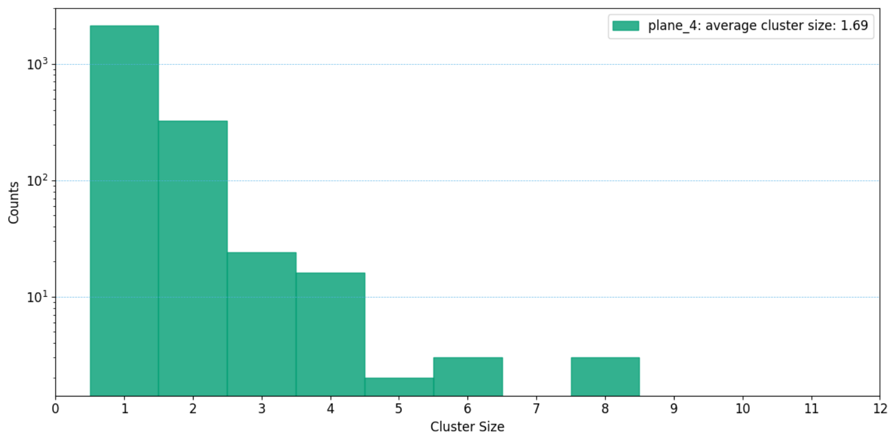

Figure 65: Cluster size distribution for plane 4.

D Lund Telescope residuals

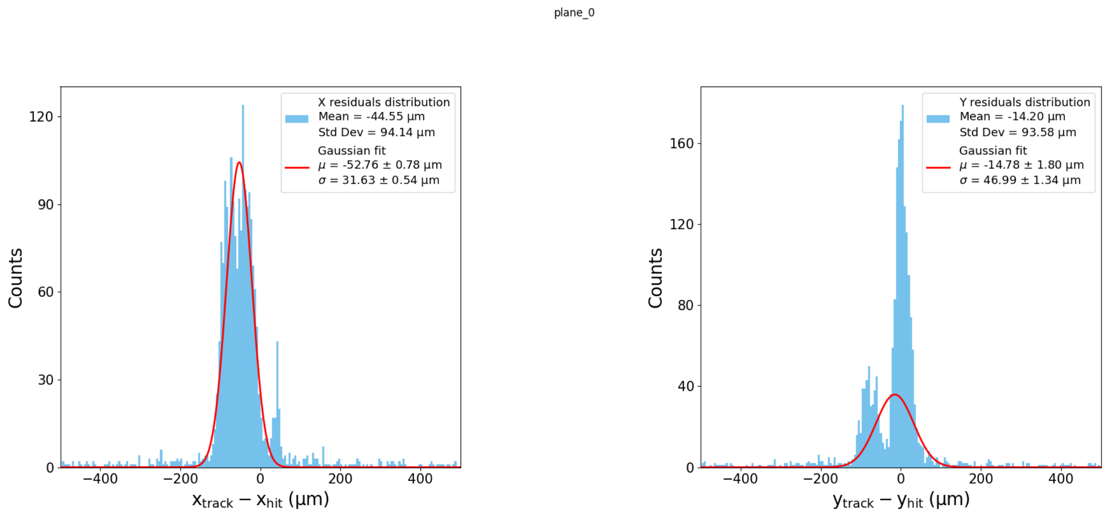

(a) Residual in X (left) and Y (right) pre-alignment

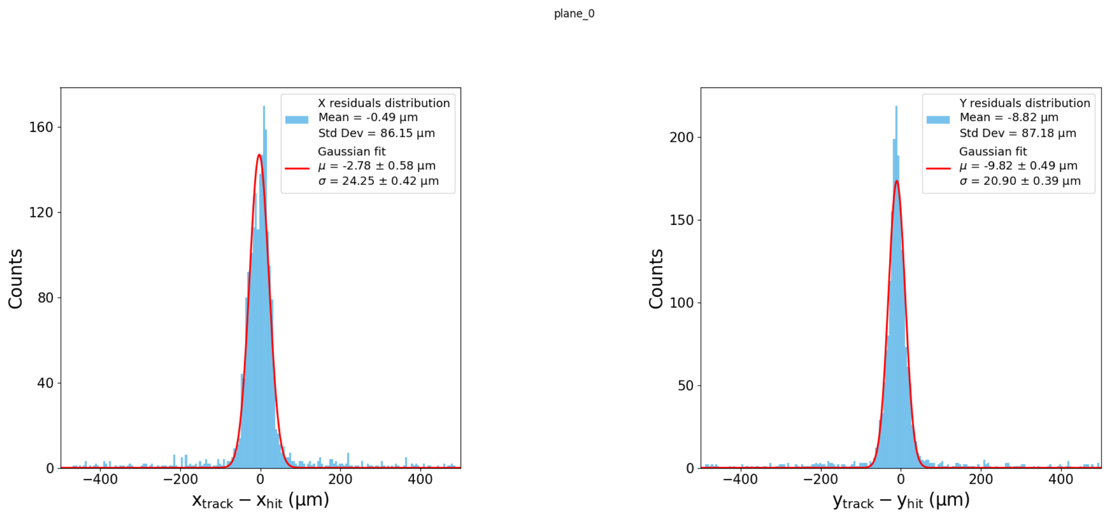

(b) Residual in global X (left) and Y (right) post-alignment

Figure 66: Residuals in X and Y of the plane 0 of Lund Telescope pre- and post-alignment.

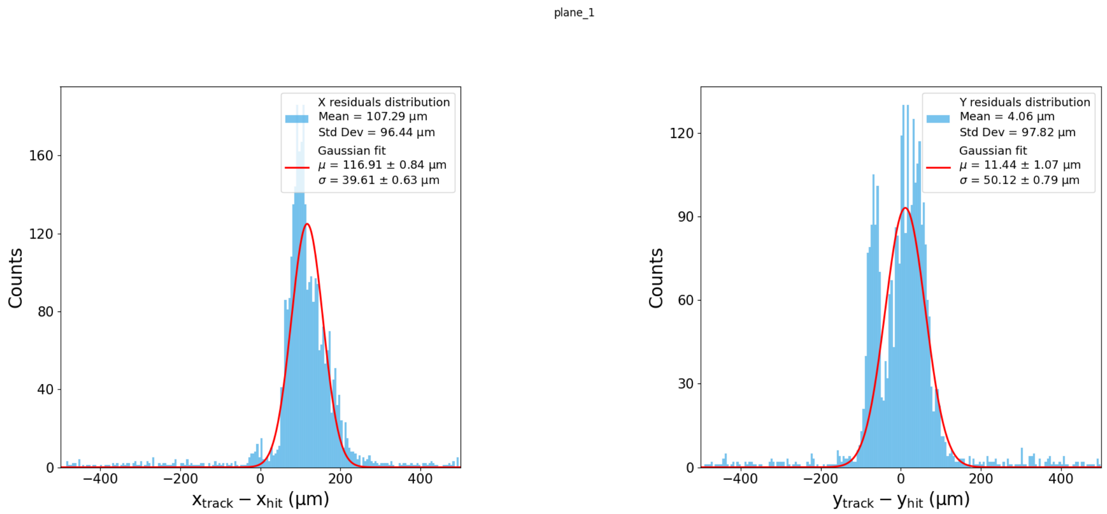

(a) Residual in X (left) and Y (right) pre-alignment

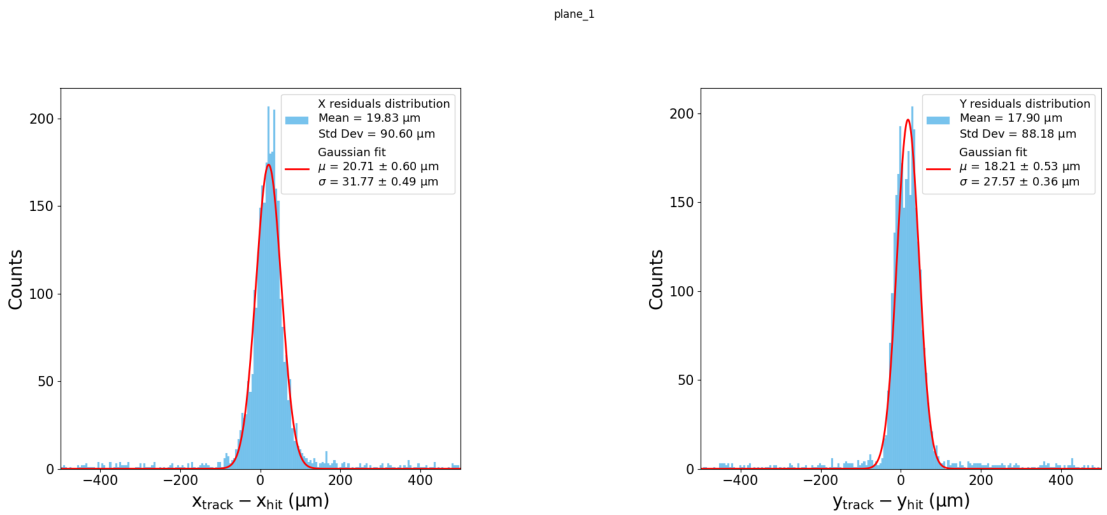

(b) Residual in global X (left) and Y (right) post-alignment

Figure 67: Residuals in X and Y of the plane 1 of Lund Telescope pre- and post-alignment.

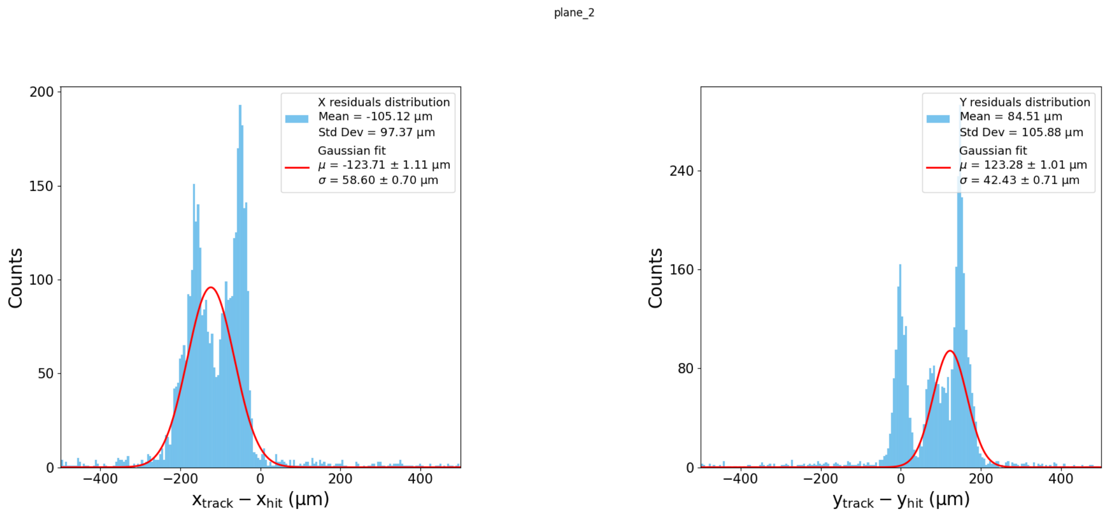

(a) Residual in X (left) and Y (right) pre-alignment

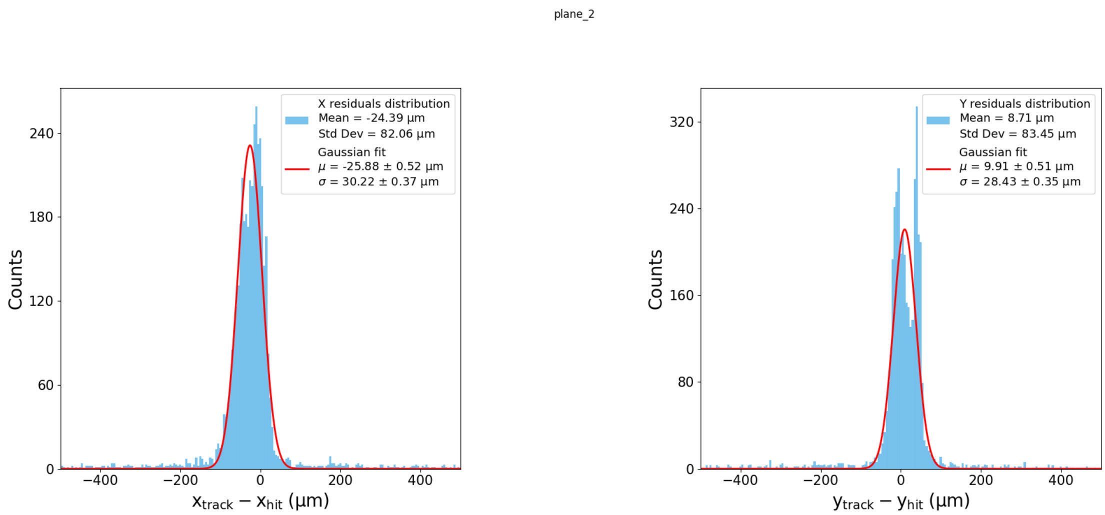

(b) Residual in global X (left) and Y (right) post-alignment

Figure 68: Residuals in X and Y of the plane 2 of Lund Telescope pre- and post-alignment.

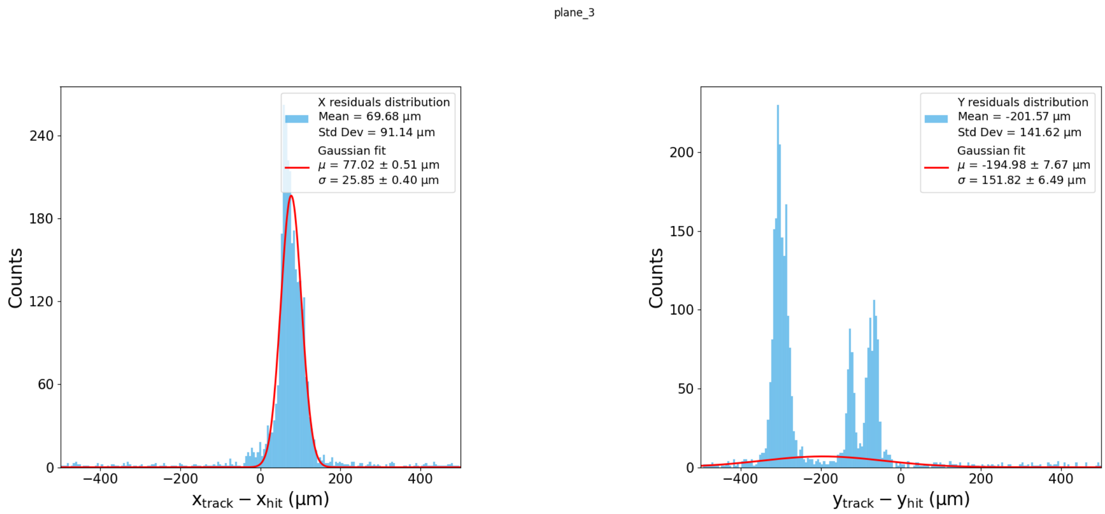

(a) Residual in X (left) and Y (right) pre-alignment

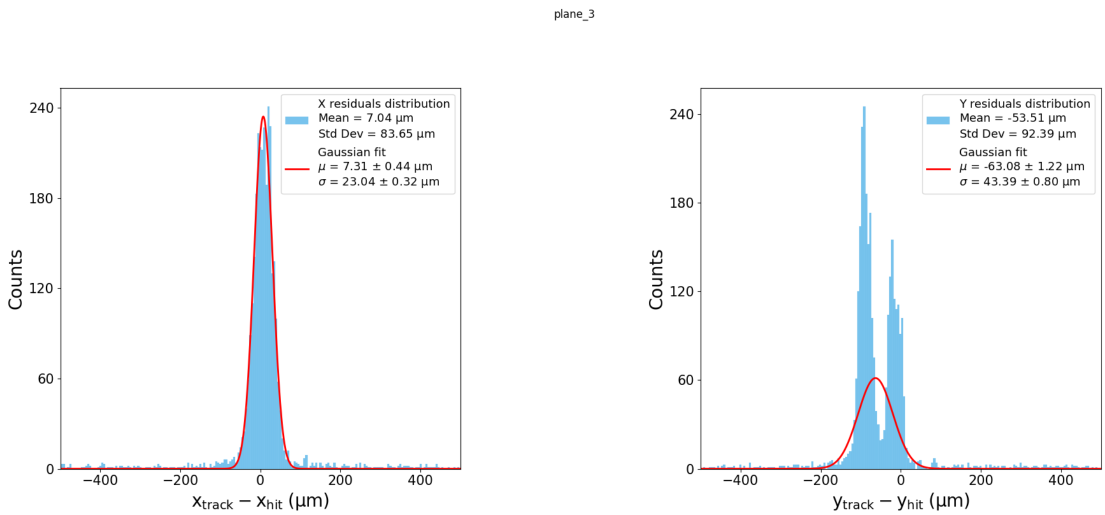

(b) Residual in global X (left) and Y (right) post-alignment

Figure 69: Residuals in X and Y of the plane 3 of Lund Telescope pre- and post-alignment.

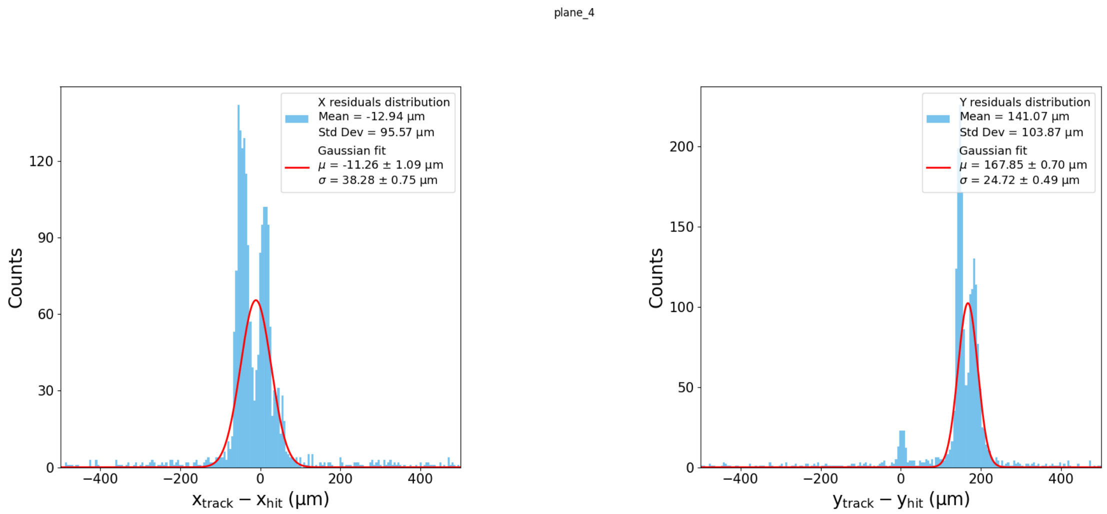

(a) Residual in X (left) and Y (right) pre-alignment

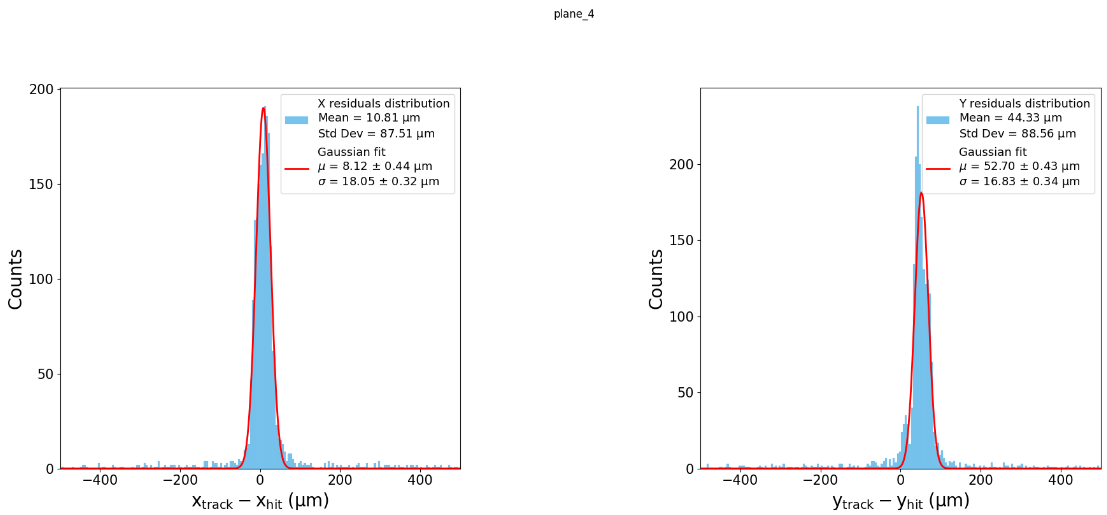

(b) Residual in global X (left) and Y (right) post-alignment

Figure 70: Residuals in X and Y of the plane 4 of Lund Telescope pre- and post-alignment.